STUDY OF FeTaN FILMS AND FeTaN LAMINATIONS STACK USING MICROWAVE TECHNIQUES

Chen Xin

(B. Sc., Hu Bei University, P. R. China)

A THESIS SUBMITTED FOR THE DEGREE OF THE MASTER OF SCIENCE

DEPARTMENT OF PHYSICS
NATIONAL UNIVERSITY OF SINGAPORE
2009

ACKNOWLEDGEMENTS

Firstly, I’d like to express my sincerest gratitude to my supervisor, Professor Ong Chong Kim for his guidance, encouragement and patience to help me in my research work. Without him, I could never have begun this project.

Secondly, my colleagues deserve to be thanked with my heart. During these two years of study, they have provided me a lot of help on microwave measurement and maintenance of facilities. Their passion and encouragement have helped me to maintain an optimistic attitude towards my experiment. Here special thanks to Dr. Ma Yungui, Dr. Liu Yan, Dr. Tan Chin Yaw, Dr. Wang Peng, Dr. Xu Feng, Dr. Zhao Li, Dr. Zhang XiaoYu, Miss Lim Siew leng, Miss Song Qing, Miss Phua Li Xian, Mr. Cheng Weining, Mr. Ning Min.

Thirdly, I thank NUS and DSO for the financial support to me and the project which I participate in these two years.

Last but not least, I would like to thank my wife, Zhang Jun for her understanding and full support during these two years study. My parents and my brother supported me from my home at China. Their encouragement and concern for me never stopped when I left home two years ago.

TABLE OF CONTENTS

SUMMARY

With the rapid development of radio frequency and microwave technologies, there are great research interests in development of soft magnetic thin films with large permeability and high resonance frequency. For the applications of electromagnetic devices, the ability to have gigahertz response with certain frequency tunability is often required. To meet these requirements, many research efforts have been placed on the controlling of the resonance frequency f_r, such as by application of stress, variation of compositions, adjusting grown parameters to fabricate samples with suitable crystallinity or post deposition treatments. Another useful approach to control the f_r is by patterning the magnetic thin films into strip structures where the resonance frequency of the magnetic film can be modified by the induced shape anisotropy. The eddy current in the patterned films can also be greatly suppressed. However, there are still few literatures that focused on the magnetic properties and microwave responses of patterned films in detail.

In this thesis, the patterning method was utilized to improve the resonance frequency of nanocrystalline FeTaN thin film, which had large permeability (10^3) up to ~1 GHz. The magnetic properties and microwave response of the patterned strip arrays were investigated at different strip widths and patterning directions.

We also deposit FeTaN thin films on flexible insulator polymer substrates and glue them together to form a composite material consisting of ferromagnetic films laminated with insulating polymer sheets. The fabrication of this kind of soft magnetic lamination stacks makes them a good candidate for high-frequency microwave device applications.

For the design of a microwave device, the complex permeability is quite critical, and they are often obtained by the conventional coaxial line method. However, it is difficult to apply the coaxial line method to measure the permeability of flat samples, which are more widely used in microwave devices. Other methods, such as equivalent LCR method and transmission line method are more feasible to measure the flat samples. In theses models, the equivalent lumped elements of the transmission line are determined from the best fit of the measurement results over the whole measurement frequency range.

In this thesis, we develop microstrip line method, and apply these methods to measure the scattering parameters of the FeTaN lamination stack. Permeability spectra of the FeTaN lamination stack are obtained by the shorted load transmission line model. In data processing procedure, the effective Permeability of the FeTaN lamination stack at different frequencies describing the transmission line is determined from the reflection measurements at different measurement frequencies. The result is examined by the full wave electromagnetic analysis combined with an optimization procedure using commercial HFSS software

LIST OF TABLES

LIST OF FIGURES

LIST OF ABBREVIATIONS AND SYMBOLS

Electric field strength vectors	E
Magnetic field strength vectors	H
Magnetic flux density	B
Electric displace vector	D
Current density vector	J
Complex permittivity	ε
Complex permeability	μ
Conductivity	σ
Surface impedance	Z_s
Reflection coefficient	R, Γ
S-parameter	S_{21}, S_{11}
Resonance frequencies	f_r
Gyromagnetic ratio	γ
Damp constant	α
Loss tangent	$\tan\delta$
Saturation magnetization	$4\pi Ms$
Uniaxial anisotropy field	H_a
Coercivity	H_c
Exchanging constant	J
Shape anisotropy field	H_k^s
Effective anisotropy field	H_k^{eff}
Series resistance per unit length	R
Series inductance per unit length	L
Shunt conductance per unit length	G
Shunt capacitance per unit length	C
Cutoff wavelength	λ_c
Guide wavelength	λ_g
Complex propagation constant	γ

Chapter 1

INTRODUCTION

1.1 Ferromagnetic materials and applications

Nowadays, microwave radars are widely used to detect distant target by transmitting and receiving reflection microwave energy. Many efforts have been made to reduce the radar signal reflected from the distant target. Normally, there are four basic techniques to minimize the microwave energy: shaping the target, using Electromagnetic (EM) absorber materials, passive cancellation and active cancellation. The first two techniques are most often applied. Shaping technique is widely employed to create a platform design with inherently low radar reflection in the primary sectors. However, it also sacrifices other properties due to abnormal shape, especially for aircraft. Coating EM absorber material onto metallic target can balance all aspect of properties for aircraft. Therefore, study of microwave absorbing material is important to minimize the radar signal.

In general, EM absorbing materials consist of dielectric or magnetic filler and polymer. Lossy dielectric materials, such as carbon and graphite, have been widely used for absorbing microwave energy in the past [1, 2, 3]. However, they are too bulky for convenient operation [4, 5]. Therefore, magnetic absorbing materials attracted more attention in recent years. Ferrites and metallic alloys are two important magnetic materials for EM absorber application.

Ferrites have many characteristic, such as low permittivity, high resonance frequency, high resistivity and good chemical stability, which are required for microwave absorbing materials. However, ferrites have high density and relative poor temperature stability, which needs to be improved.

Compared with ferrite, metal materials have larger saturation magnetization and high complex permeability, which make its possible to reducing the thickness of microwave absorber [6, 7]. Ferromagnetic powders, such as Fe-Si-N, and Fe, Co, Ni, have been widely studied as absorbing material [8, 9]. However, the electric conductivity of these materials is high. Furthermore, the permittivity is very large, which make it difficult to satisfy impedance match between the EM material and air in free space. Therefore, our research is focused in studying the ferromagnetic lamination stack to match impedance and reduce conductivity for microwave absorption.

1.2 Scope of study

1.2.1 Maxwall's equations

Maxwall's equations describe the response of a material to electromagnetic fields [10]:

$$\nabla \cdot \vec{D} = \rho \qquad (1.1)$$

$$\nabla \cdot \vec{B} = 0 \qquad (1.2)$$

$$\nabla \times \vec{H} = \partial \vec{D} / \partial t + \vec{J} \qquad (1.3)$$

$$\nabla \times \vec{E} = \partial \vec{B} / \partial t \qquad (1.4)$$

With the following constitutive relations:

$$\vec{D} = \varepsilon \vec{E} = (\varepsilon' - j\varepsilon'')\vec{E} \qquad (1.5)$$

$$\vec{B} = \mu \vec{H} = (\mu' - j\mu'')\vec{H} \qquad (1.6)$$

$$\vec{J} = \sigma \vec{E} \qquad (1.7)$$

Where $\vec{E}$ and $\vec{H}$ are the electric field and magnetic field strength vectors, separately. $\vec{B}$ is the magnetic flux density. $\vec{D}$ is the electric displacement vector. $\vec{J}$ is the current density vector. ρ is the density of charge. $\varepsilon = \varepsilon' - j\varepsilon''$, is the complex permittivity of the material. $\mu = \mu' - j\mu''$, is the complex permeability of the material; σ is the conductivity of the material.

The above equations show that the responses of electromagnetic materials are characterized by three parameters, ε, μ, and σ. These parameters also determine the spatial extent to which the electromagnetic field energy can penetrate into the material at a given frequency. At microwave frequencies, the penetration depth of conductors is small that the interaction may be limited to the surface only. Hence the utility and behavior of conductors at microwave frequencies are mainly determined by their surface impedance Z_S:

$$Z_s = E_t / H_t = R_s + jX_s \qquad (1.8)$$

Where E_t and H_t are the tangential electric field and tangential magnetic field. R_s is the surface resistance, and X_s is the surface reactance. At microwave frequency, the skin depth of metallic material is of the order of a few microns and the field cannot penetrate the material, which means the pure metallic magnetic materials cannot be used as absorber. Furthermore, most microwave energy will reflect at interface between air and metal as shown in Fig.1.1. Therefore, our research is focused on the composite of metallic magnetic films with the dielectric substrate and epoxy to form electromagnetic materials.

1.2.2 Microwave reflection in free space

The reflection coefficient is used in electromagnetic absorber when microwave propagation in free space containing discontinuities is considered. A reflection coefficient R describes the intensity of a reflected wave relative to an incident wave.

$$R = \frac{Z_{in} - Z_0}{Z_{in} + Z_0} \qquad (1.9)$$

Where Z_0=1, is the impedance in free space and Z_{in} is the impedance of the load, it is determined by

$$Z_{in} = \sqrt{\frac{\mu}{\varepsilon}} \tanh(-i2\pi f \sqrt{\mu\varepsilon d}) \qquad (1.10)$$

Where ε and μ are the relative complex permittivity and permeability of the absorber materials, d is the width of the absorber materials along the microwave propagation direction. In order to make the incident EM wave to penetrate into absorber but not being reflected at interface, it needs adjusting the μ′/ε′ (close to 1) and d values are adjusted to reduce the impedance mismatch at the interface between absorber and air. After the microwave propagating into the absorber, strong absorption is based on a large μ″ of absorber material near resonance frequency.

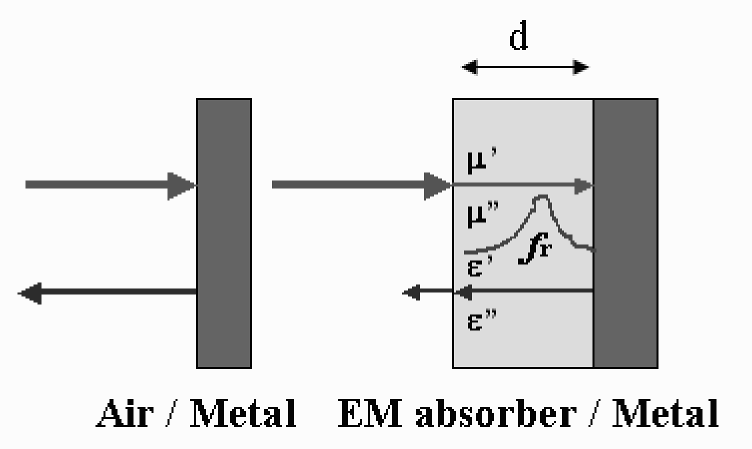

Figure 1.1 Reflection at interface with and without EM absorber in free space

1.2.3 General properties of material

To find the possible candidate material for EM absorber, we need to introduce the material classification of natural material. Normally, material can be classified as dielectrics, magnetic materials, semiconductors, and conductors according to their ε, μ, and σ values.

i. Dielectrics

Dielectrics are materials with high resistance. A possible behavior of ε′ and ε″ as a function of frequency are shown in Fig.1.2 [11]. ε″ will reach maximum at a frequency f_m, which is related a characteristic time: $\tau = \frac{1}{2\pi f_m}$ according to Debye equations, the permittivity equals:

$$\varepsilon' = \varepsilon_\infty + \frac{\varepsilon_s - \varepsilon_\infty}{1+\omega^2\tau^2} \qquad (1.11)$$

$$\varepsilon'' = \frac{(\varepsilon_s - \varepsilon_\infty)\omega\tau}{1+\omega^2\tau^2} \qquad (1.12)$$

Where ε_s and ε_∞ are the limiting values of the relative permittivity connected with the dispersion at $\omega\tau \ll 1$, $\omega\tau \gg 1$, respectively. The maximum value of permittivity is, $\varepsilon''_m = \frac{\varepsilon_s - \varepsilon_\infty}{2}$, when $\omega\tau = 1$.

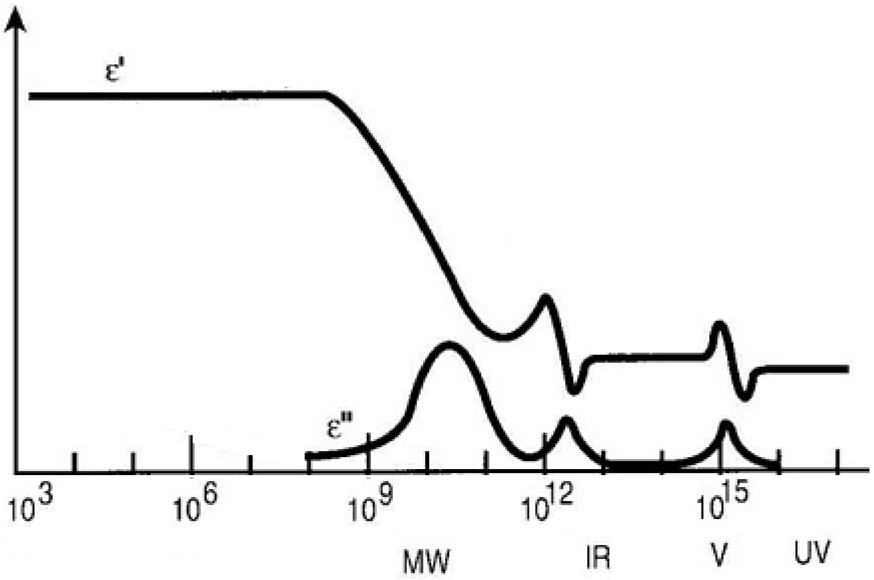

Figure 1.2 Frequency response of permittivity for a hypothetical dielectric [12]

ii. Magnetic materials

The typical magnetic spectrum is shown in Fig. 1.3. In low frequency range ($f<10^6$ Hz), μ′ and μ″ change a little. In the high frequency range ($10^6<f<10^8$ Hz), μ′ decrease quickly, and μ″ increase greatly. In the ultra-high frequency range ($10^8<f<10^{10}$ Hz), natural resonances occur and μ″ have maximum value.

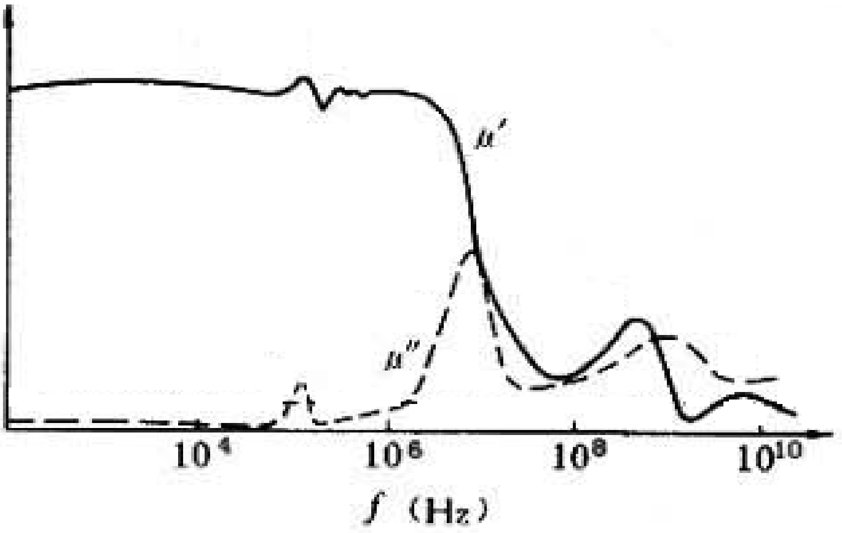

Figure 1.3 Typical magnetic spectrum of ferromagnetic materials [13]

iii. Conductors

Conductors are very conductive. The permittivity of conductor is:

$$\vec{\varepsilon} = \varepsilon + i\frac{\sigma}{\omega} \qquad (1.13)$$

Where σ is the conductivity of conductor and the permittivity of the conductor are far larger than dielectric materials. For example, the relative static permittivity of Aluminum at 10 kHz is about $-1300+ i\times1.3\times10^{14}$.

iv. Semiconductors

The resistance of semiconductor is lower than that of a dielectric. Normally, the resistance of semiconductor is in the range of 10^{6}-10^{-2}(Ωm).

1.3 The objective of the study

In our work, we study the effect of patterning ferromagnetic films in controlling the resonance frequency in microwave frequency range. The properties of ferromagnetic film lamination stack structure as EM absorber are investigated. Different microwave measurement methods were employed to characterize the complex permittivity and complex permeability of stack and other materials.

A brief outline of this thesis is given as follows:

First, a brief introduction about this study, including applications, background information and our motivations, is given in Chapter 1. For this research, microwave measurement is required for the evaluation of single layer FeTaN thin film. Therefore, Chapter 2 will be preceded with the introduction of experimental techniques used in this work, including the samples fabrication, characterization techniques. In Chapter 3, we study the patterning methods for tuning ferromagnetic resonance peak of single layer FeTaN thin film. Based on these investigations, we design and fabricate FeTaN lamination stack to study its electric and magnetic properties. Thus Chapter 4 will introduce the detailed lamination stack structure in this study and corresponding measurement methods. Finally, the thesis is completed with Chapter 5, conclusion about the FeTaN thin film and FeTaN lamination stack properties and measurement method.

References

[1] W.H. Emerson, IEEE Trans. Antenna & Propag. **21**, 484 (1973).

[2] P.T.C. Wong, B. Chambers, A.P. Anderson and P. V. Wright, Electron Lett. **28**, 1651 (1992).

[3]K. Naishadham and P.K. Kadada, IEEETrans. Microw. Theory & Tech. **39**, 1158 (1991).

[4] Y. Natio and K. Suetake, IEEE Trans. Microw. Theory & Tech. **19**, 65 (1971).

[5] K. J. Vinoy and R. M. Jha, Radder Absorbing Materials ED. R.m. Jha, (Kluwer academic publishers), 108 (1996).

[6] S. Yoshida, M. Sato, E. Sugawara and Y. Shimada, J. Appl. Phys. **85**, 4636 (1999).

[7] T. Maeda, S. Sugimoto, T. Kagotani, D. Book, M. Homma, H. Ota and Y. Houjou, Mater. Trans. JIM **41**, 1172 (2000).

[8] L. Olmedo, G. Chateau, C. Deleuze and J.L. Forveille, J. Appl. Phys. **73**, 6992 (1993).

[9] G. Viau, F. Ravel, O. Acher, F. Fievet-Vincent and F. Fievet, J. Appl. Phys. **76**, 6570 (1994).

[10] D. M. Pozar, Microwave Engineering (Wiley, New York, 2005).

[11] S. Ramo, J. R. Whinnery, and T. Van Duzer, Fields and Waves in Communication Electronics (Wiley, New York, 1994).

[12] J. Smit, Magnetic Properties of Materials (McGraw-Hill, New York, 1971)

Chapter 2

EXPERIMENTAL TECHNIQUES

2.1 FeTaN films deposition system

There are several options for fabricating films, such as pulsed laser deposition (PLD), sputtering, physical vapor deposition，sol-gel and metal-organic chemical vapor deposition [1-7]. The deposition techniques used in this thesis are RF magnetic sputtering system.

RF magnetic sputtering system is a thin film deposition which is one of a physical vapor deposition (PVD) technique. This deposition method uses an ultra-high voltage which is focused in the target surface to ionize the argon atom. And the positive Argon ion will accelerate by this high electric field and strike on a target of the desired composition. Material is then vaporized from the target and deposited as a thin film on a substrate. This process can occur in ultra high vacuum or in the presence of a background gas.

Figure 2.1 shows the diagram of a typical magnetic sputtering system. We used the commercial target holder system (AJA Company). Two different target holders are inside the chamber. This would enable us to grow different thin film layers without breaking the vacuum by changing the desired target holders. This would also help to keep the sample clean during the deposition. The distance between the target and the sample is around 25 cm. The chamber can be pumped down to a vacuum of around 3×10^{-7} Torr by a turbo molecular pump backed by a rotary pump.

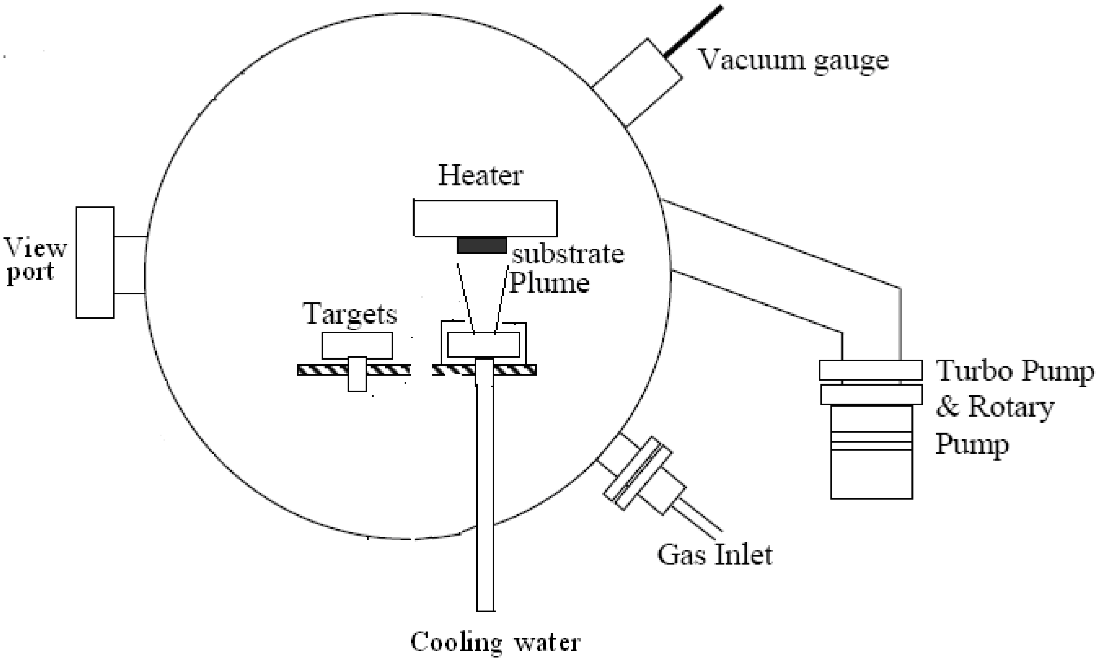

Figure 2.1 A schematic drawing of the RF magnetic sputtering system.

All the FeTaN thin film samples mentioned in this dissertation were deposited on 0.5mm thick Si substrate and 8μm thick Mylar substrate. It is necessary for the substrate surface to be very clean prior to the deposition process to ensure fabrication of good quality thin film. The substrate was cleaned by first immersing it in an acetone and ethanol (purity > 99.8 %) ultrasonic bath for 10 minutes to remove organic contaminants. The substrate was then stored in high purity ethanol (> 99.9 %) until it is ready to be loaded into the vacuum chamber. Before loading into the chamber, the substrate was blown dry using compressed nitrogen gas. The substrates were adhesively attached to sample holder (resistive heater) by applying double-side tape.

2.2 Scattering parameters from vector network analyzer (VNA)

VNA is widely used in microwave frequency applications to measure the complex scattering (S) parameters of an unknown DUT [8]. Two-port measurement technique, called transmission line technique, is commonly used in high-frequency measurements, as shown in Fig. 2.2. The amount of energy that is reflected and transmitted is expressed as S-parameter. Fig. 2.2 show how the S-parameters are defined, where S_{11} is reflection a port 1 with port 2 matched, S_{21} is forward transmission with port 2 matched, S_{12} is reverse transmission with port 1 matched, and S_{22} is reflection at port 2 with port 1 matched.

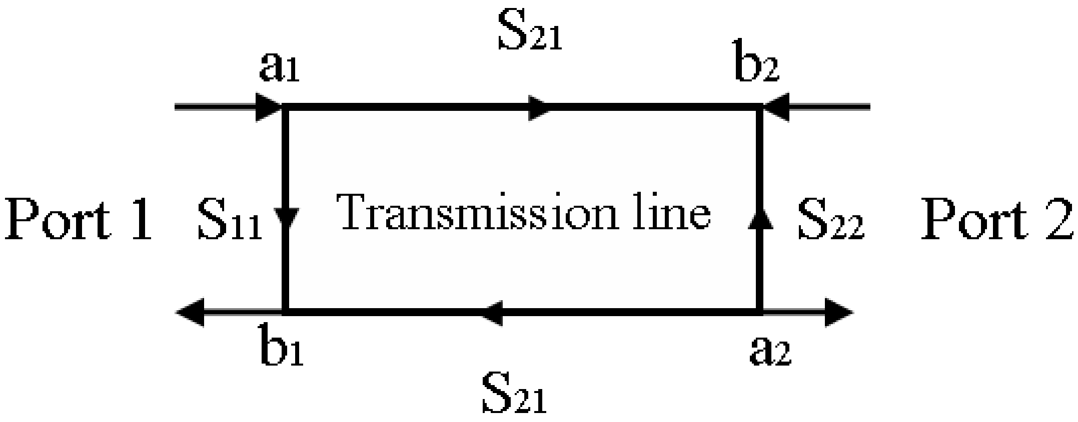

Figure 2.2 Scattering parameter of a two port device

Once the S-parameters have been found, they can be converted into the complex EM properties of the material, such as the complex permittivity ε and permeability μ, which will be discussed in chapter 4.

Before measuring the sample, the VNA will connect with standard open, short, and load terminators calibration kit to decrease the system errors in VNA. To check the calibration, an empty sample holder can be measured first. If the test of the empty sample holder showed a permittivity and permeability near 1, the calibration is completed and the VNA facility is ready for use.

Reference

[1] S. Otsubo, T. Maeda, T. Minamikawa, Y. Yonezawa, A. Morimoto and T. Shimizu , Jpn. J. Appl. Phys. Part 2 **29** 133, (1990).

[2] H. Buhay, S. Sinharoy, W.H. Kanser, M.H. Francombe, D.R. Lampe and E. Stepkee, Appl. Phys. Lett. **58,** 1470 (1991).

[3] D. Roy, S. B. Krupanidhi and J. P. Dougherty, J. Appl. Phys. **69,** 7930 (1991).

[4] K. D. Budd, S. K. Dey and D. A. Payne, Br. Ceram. Proc. **36**, 107 (1985).

[5] S. B. Majumder, D. C. Agrawal, Y. N. Mohapatra and V. N. Kulkarni, Int. Ferro. **8**, 217 (1995).

[6] M. Ichiki, J. Akedo, A. Schoroth, R. Maeda, Y. Ishikawa, Jpn. J. Appl. Phys. **36**, 5815 (1997).

[7] C. Lucat, F. Menil, and R. R Von Der Mühll, Mea. Sci. & Tech. **8**, 38 (1997).

[8] D. M. Pozar, Microwave Engineering (Wiley, New York, 2005).

Chapter 3

PATTERNING METHOD

For the applications of electromagnetic devices, the ability to have gigahertz response with certain frequency tunability is often required. To meet these requirements, many research efforts have been placed on the controlling of the resonance frequency (f_r) [1-4], such as by application of stress [5-8], variation of compositions [9-12], adjusting grown parameters to fabricate samples with suitable crystalline or post-deposition treatments [13-15]. Another useful approach to control the f_r is by patterning the magnetic thin films into strip structures where the resonance frequency of the magnetic film can be modified by the induced shape anisotropy [16-20]. The eddy current in the patterned films can also be greatly suppressed. In this chapter, the magnetic properties and microwave response of the unpatterned and patterned FeTaN films are observed.

3.1 Strips patterned with one strip width period

In this chapter, the magnetic properties and microwave response of the patterned FeTaN strip arrays were investigated at different strip widths and patterning directions. Figures 3.1(a) and 3.1(b) show the schematics of two kinds of strip arrays patterned with strip directions parallel and perpendicular to the easy magnetization axis (the y axis) of the unpatterned film, respectively. The film normal direction is defined along the z axis and the exciting rf magnetic field is applied along the x axis parallel to the hard axis of the unpatterned film.

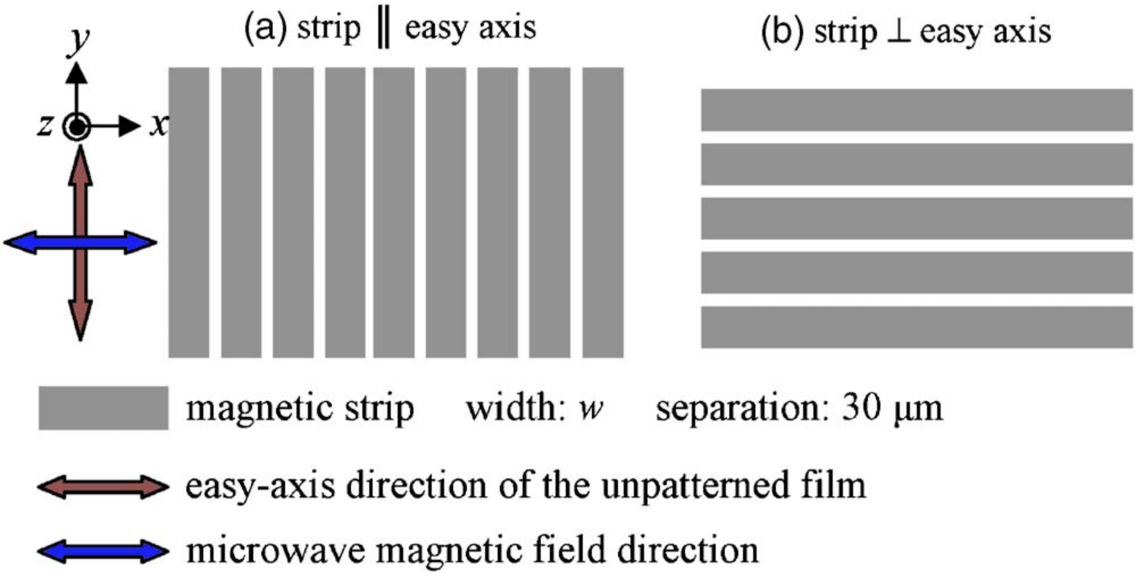

Figure 3.1 (Color online) Schematic structure of the strip arrays patterned along the easy (a) and hard (b) axes of the unpatterned film together with the coordinate system. The easy axis of the unpatterned film is along the *y* axis and the microwave measurement is applied with the magnetic field along the *x* axis.

3.1.1. Strips patterned along the easy axis with different strip width

FeTaN thin films were grown on (100) silicon substrates of dimensions of $5\times10\times0.5\text{mm}^3$ by rf magnetron sputtering. The sputtering target was a 3 inch iron disk with 6% of the surface area covered by tantalum chips. A 120 Oe magnetic field was applied along the short edge of the substrates to induce an in-plane uniaxial anisotropy. The sputtering chamber was evacuated to a base pressure of 3×10^{-7} Torr. Ar + (3%) N2 gas mixture was used as the ambient sputtering gas and the deposition pressure was maintained at 1 mTorr. The rf power was 80 W. The thickness of FeTaN thin film was controlled at about 100 nm. Conventional UV photolithography method was used to fabricate the patterns. Wet etching method was used to etch the FeTaN thin films with a mixture of diluted nitric acid and hydrochloric acid as the etchant. Magnetic strips of widths=30, 60, 150, 500 μm and separation gap of 30 μm were fabricated with the directions parallel to the easy magnetization axis (the y axis) of the unpatterned film. The patterned structures are schematically shown in Fig. 3.1. The static magnetic property of the FeTaN thin films was measured using a BH-loop tracer. The permeability spectrum was measured using a homemade microstrip transmission-line perturbation method with the rf magnetic field along the x axis.

According to Kittel's formula [21], the ferromagnetic resonance frequency of the strips patterned along the easy axis as shown in Fig. 3.1 can be theoretically predicted by

$$f_r = \frac{\gamma}{2\pi\sqrt{1-\alpha^2}}\sqrt{4\pi M_S(H_a + 4\pi M_S)} \qquad (3.1)$$

where γ is the gyromagnetic ratio (=1.76×10^{11} T^{-1} s^{-1}), α is the damp constant, H_a is the uniaxial anisotropy field of the unpatterned film, ε is the effective demagnetization factor, and $4\pi Ms$ is the saturation magnetization. The theoretical values for the permeability can be calculated by Landau–Lifshitz–Gilbert equation by the formula

$$\mu = 1 + \frac{4\gamma M_S^2(f_r^2 - f^2 - j2\alpha f_r f)}{(f^2 - f_r^2)^2 + 4\alpha^2 f^2 f_r^2} \qquad (3.2)$$

Figures 3.2(a) and 3.2(b) show the easy- and hard-axis hysteresis loops of the unpatterned film and the strip arrays patterned along the easy axis at the selected strip widths of w =30, 60, and 150μm. It is seen that the unpatterned film has a well-defined uniaxial anisotropy. The typical magnetic parameters read from the hysteresis loops are 4πMs=2.0 T, $H_{ce}\approx H_{ch}$=4.5 Oe, and H_k=12 Oe. Here, H_{ce} and H_{ch} are the easy- and hard-axis coercivities, respectively, and $H_k = (H_a+4\pi\varepsilon Ms)$ is the effective anisotropy field obtained from the cross point of the central line of the low-field portions of the hard-axis loop with the counter extension of the magnetization saturation line. After patterning, the easy-axis loop shows little changes, indicating that the domain wall motion for the magnetization reversal in this direction was not influenced by the patterning. It is possible because the strip width is far larger than the domain wall width (>2μm) at least by two orders. The slopes of the hard-axis loops are gradually increased as the strips become narrower, indicating the increase in the effective anisotropy field after patterning. For the strips of w=30 μm, the estimated H_k is about 36 Oe, which has two times increment compared with the unpatterned film. Thus, the validity of the patterning method to increase the magnetic anisotropy is evidenced.

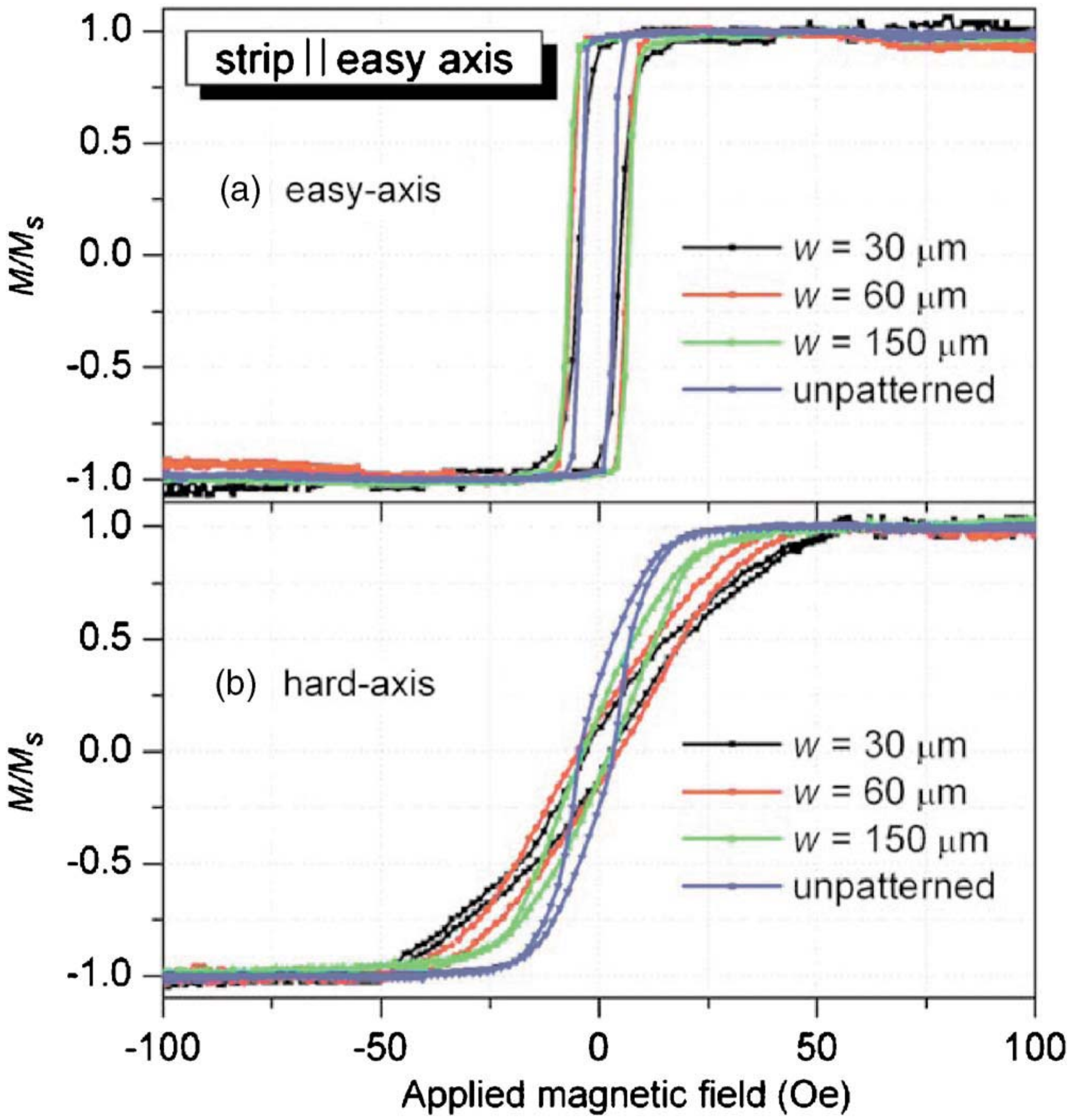

Figure 3.2 (Color online) (a) Easy- and (b) hard-axis hysteresis loops of the unpatterned film and the films patterned along the easy axis of the unpatterned film at the selected strip widths of *w*=30, 60, and 150 μm.

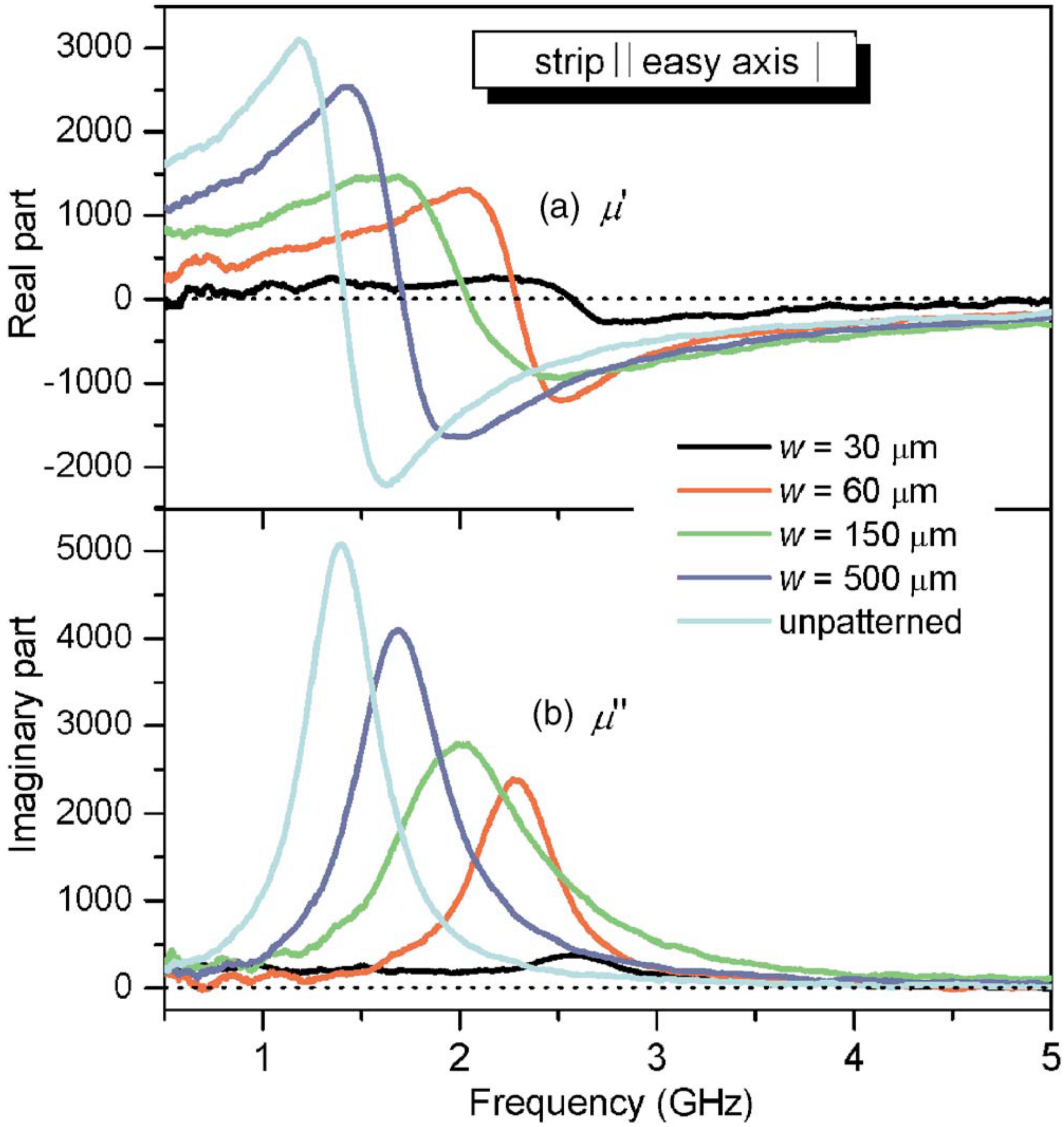

Figure 3.3 (Color online) Real (μ') (a) and imaginary parts (μ'') (b) of the permeability of the unpatterned film and the strips at widths of w=30, 60, 150, and 500 μm.

Figures 3.3(a) and 3.3(b) show the real (μ') and imaginary parts (μ'') of the permeability of the unpatterned film and the strips of widths w=30, 60, 150, and 500 μm, respectively. The unpatterned film has a resonance frequency f_r =1.38 GHz with μ' of 1500–3000 at f < f_r and μ'' of ~5000 at f_r. The rapid increase of μ'' at f_r indicates the film has a low damp constant α. For the patterned strips, the resonance frequency shifts toward larger values and the permeability decreases when the strip width is narrowed. These results are consistent with the magnetic properties of the strips as predicted by Eqs. (3.1) and (3.2). The 30μm strips have a resonance frequency of 2.58 GHz, nearly one time larger than that of the unpatterned film. Table 3.1 lists the typical magnetic parameters including the effective anisotropy field (H_k), the resonance frequencies calculated (f_r^{calc}) and measured (f_r), and the real μ' and imaginary parts μ" of permeability of the strips at different widths patterned along both the easy and hard axes of the unpatterned film. f_r^{calc} is obtained from Eq. (3.1) with H_k read from the hard-axis hysteresis loop. The theoretical prediction can well agree with the measured results at $w < 30\mu m$. It confirms the validity to approximate the shape anisotropy in the wide strip by an average demagnetization factor. For the 30μm strip, the magnetization reversal becomes more inhomogeneous, as evidenced by the hard-axis hysteresis loop in Fig. 3.2(b). It degrades the accuracy of the current model, which assumes a continuous domain rotation.

TABLE 3.1. Typical magnetic parameters of the strips at different widths patterned along the easy and hard axes of the unpatterned film. It includes the effective anisotropy field (H_k), the calculated (f_r^{calc}) and measured (f_r) resonance frequencies, and the real μ' and imaginary parts μ" of the permeability. The width of ∞ denotes the unpatterned film f_r^{calc} is calculated from Eq. (3.2).

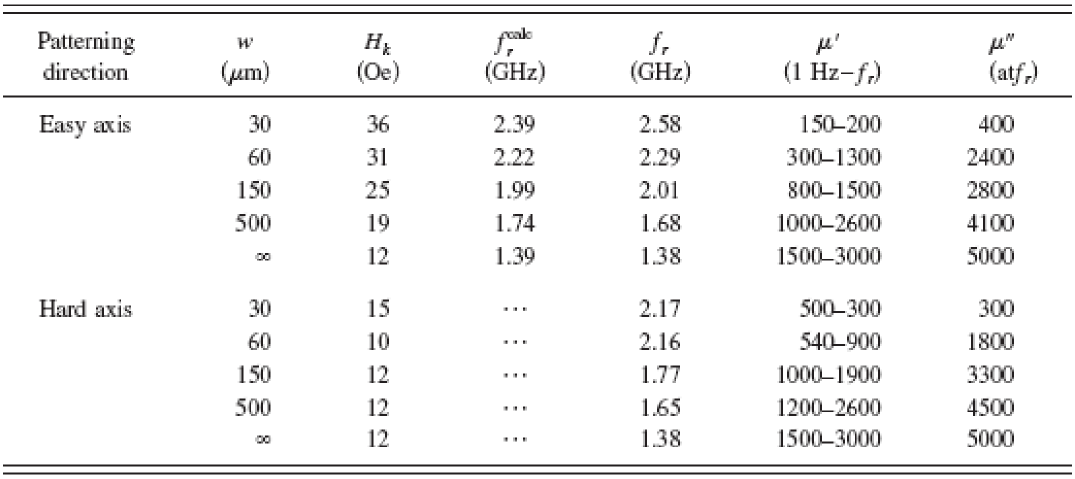

Patterning direction	w (μm)	H_k (Oe)	f_r^{calc} (GHz)	f_r (GHz)	μ' (1 Hz$-f_r$)	μ'' (atf_r)
Easy axis	30	36	2.39	2.58	150–200	400
	60	31	2.22	2.29	300–1300	2400
	150	25	1.99	2.01	800–1500	2800
	500	19	1.74	1.68	1000–2600	4100
	∞	12	1.39	1.38	1500–3000	5000
Hard axis	30	15	⋯	2.17	500–300	300
	60	10	⋯	2.16	540–900	1800
	150	12	⋯	1.77	1000–1900	3300
	500	12	⋯	1.65	1200–2600	4500
	∞	12	⋯	1.38	1500–3000	5000

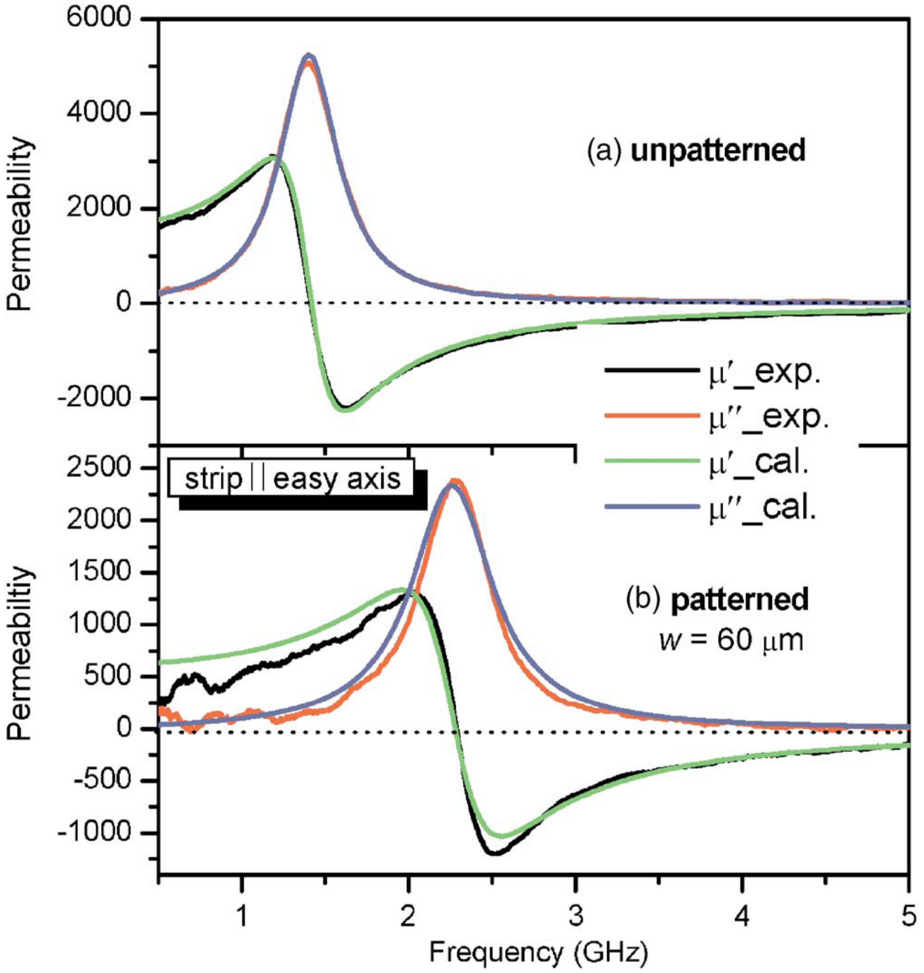

Figure 3.4. (Color online) Measured and calculated permeability spectra for the unpatterned film (a) and the film patterned at w=60 μm (b). The parameters used for calculation by Eq. 3.2 are $4\pi Ms$= 2.0T, H_a= 12Oe, α= 0.15, and ε= 0.001.

Figures 3.4(a) and 3.4(b) show the measured and calculated permeability spectra for the unpatterned film and the strip array of w=60 μm, respectively. The parameters for calculation are $4\pi Ms$= 2.0 T, H_a=12 Oe, α=0.15, and **ε**=0.001. For the unpatterned film, the calculated result is reasonably consistent with the experimental data. For the patterned strips, the calculated values also well accord with the experimental data although its real part is a little larger at $f < f_r$. Therefore, the average demagnetization factor model is effective to describe the microwave response of the magnetic strip, which has a homogeneous domain.

3.1.2. Strips patterned along the hard axis with different strip width

Figures 3.5(a) and 3.5(b) show the easy- and hard-axis hysteresis loops of the unpatterned film and the films patterned along the hard axis at the selected strip widths of *w*=30, 60, and 150μm. As shown in Fig. 3.5(a), the easy-axis loop becomes sheared as the strip width is decreased. It is expected because the strengthened demagnetization effect in narrower strips decreases the nucleation field for the formation of the initial reversed domains. The hard-axis loop in Fig. 3.5(b) shows little changes as the strip width is reduced from 500 to 60 μm. It can take place when enclosed domains are formed inside the strips where no demagnetization field exists in the film plane. For the strips of width w=30 μm, the saturation field is greatly increased although the effective anisotropy field evaluated from the low-field loop has no much difference from the wider strips, as listed in Table 3.1.

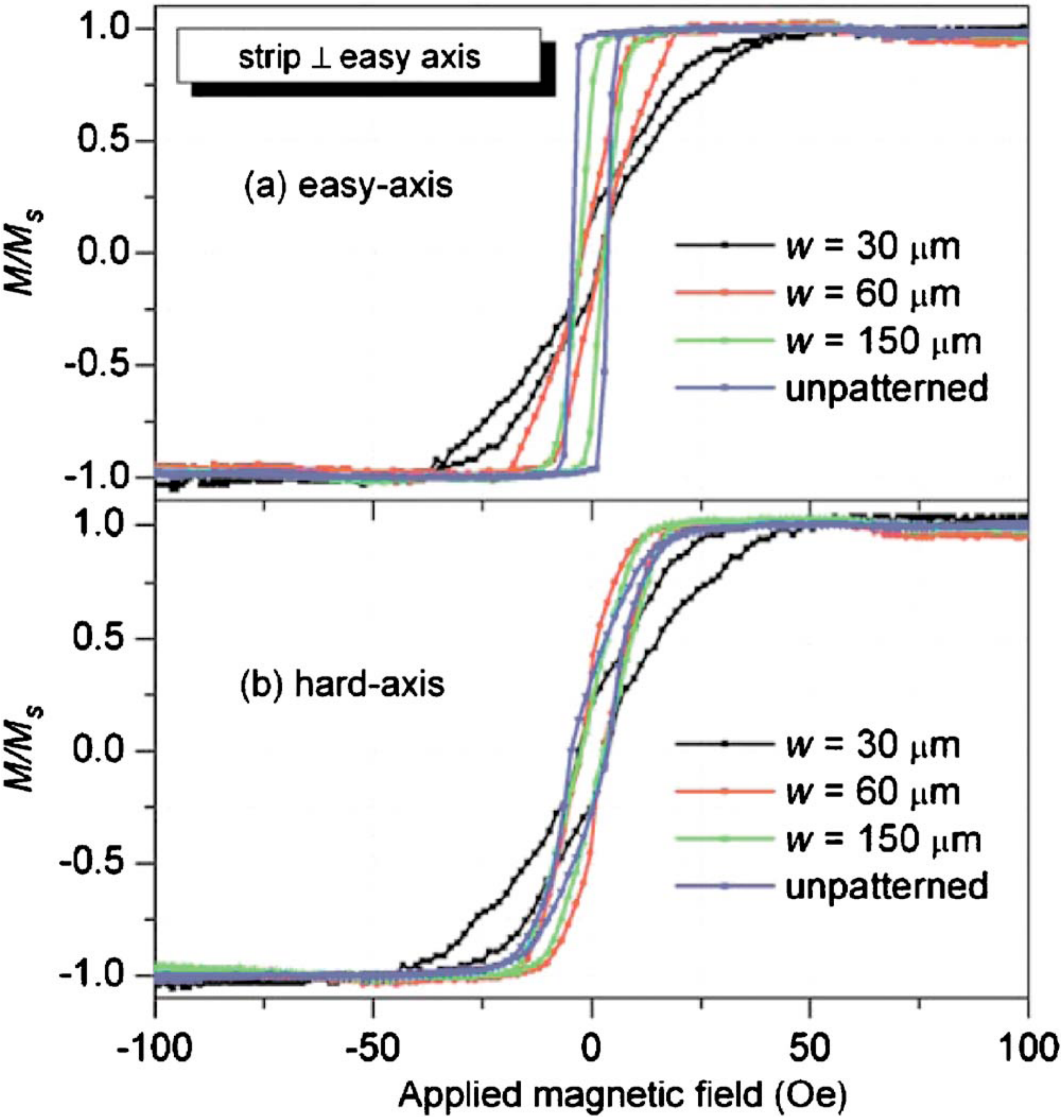

Figure 3.5. (Color online) (a) Easy- and (b) hard-axis hysteresis loops of the unpatterned film and the films patterned along the hard axis of the unpatterned film at the selected strip widths of *w*=30, 60, and 150 μm.

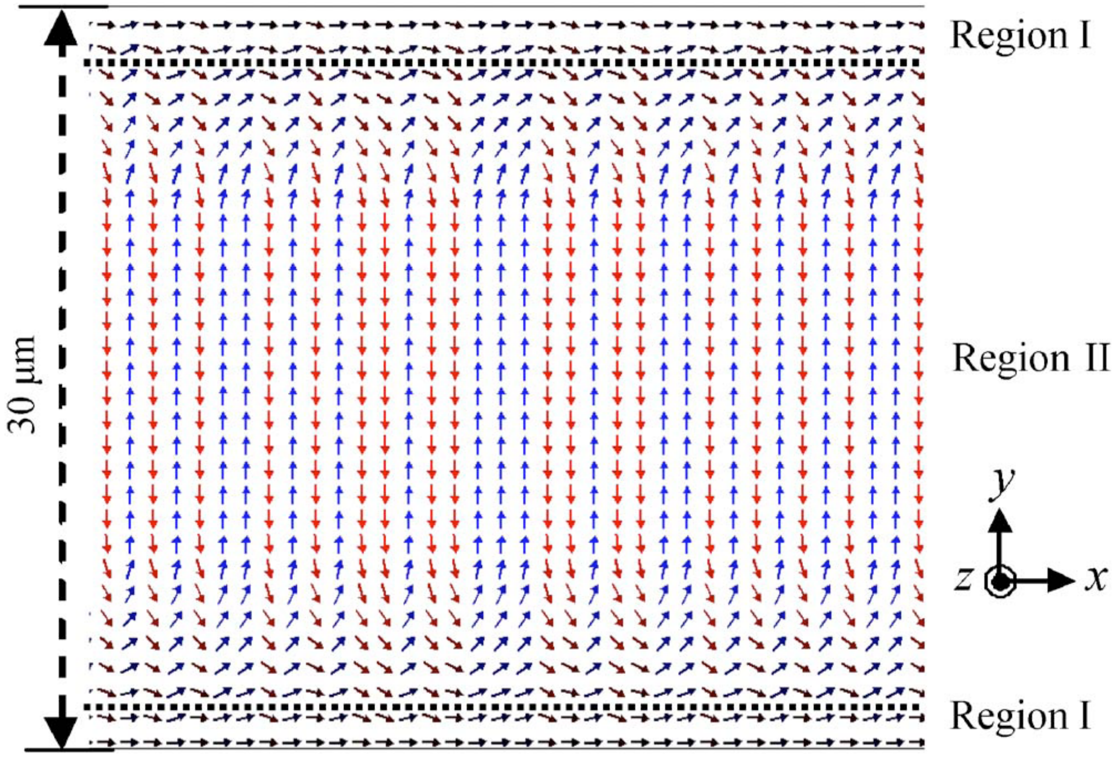

Figure3.6. (Color online) Prediction of the remanent magnetization distributions in one segment of the 30 μm FeTaN strip calculated by OOMMF. The parameters used for calculation are 4πMs=2.0 T, exchanging constant J=2×10^{-11} J /m, effective anisotropy energy K=10^3 J/m^3, damp constant α=0.15, the unit cell size 0.25×0.25×0.1μm^3, and the calculated sample dimension 300×30×0.1 μm^3.

Figure 3.6 gives a theoretical prediction of the remanent magnetization distributions in one segment of a 30 μm FeTaN strip calculated by OOMMF software. The parameters used for calculation are 4πMs=2.0 T, exchanging constant J=2×10^{-11} J /m, effective anisotropy energy K=10^3 J/m^3, damp constant α=0.15, the unit cell size 0.25×0.25×0.1μm^3, and the calculated sample dimension 300×30×0.1 μm^3. Confined by the computer resource, the cell size selected is actually larger than the single domain wall dimension. The magnetostatic interaction between the strips is also neglected, which will be important for the strips of narrower spacing. Thus, the calculated domain pattern will be referred as a rough guide. As shown in Fig. 3.6, two types of domains can be roughly recognized: one is the homogenous single domain formed near the strip edges as denoted by region I where magnetizations are oriented parallel to the strip edges, and the other is the “S-shaped” domains formed in the rest part of the strip as denoted by region II. For such a complex domain pattern, there should be no demagnetization field in the film plane. These two types of domains have different magnetization reversal processes, which can be recognized from the hysteresis loops. However, the magnetization contribution from region I can be manifest only in a narrow strip where it has a comparable volume with region II. It should be the case for the 30 μm strip where the hard-axis loops becomes more sheared, as shown in Fig. 3.5(b). On the other hand, the easy-axis loop is sensitive to the strip width even at w=30μm. It is because domain reversal in this direction is mainly controlled by wall motion and the demagnetization field induced in the strips facilitates the formation of initial reversed domains and their successive expansion.

Figures 3.7(a) and 3.7(b) show the real μ' and imaginary parts μ" of the permeability of the unpatterned film and the strips patterned along the hard axis at widths w=30, 60, 150, and 500 μm, respectively. The resonance frequency of the strips shifts toward larger values and the permeability reduces as the strip width is decreased. These width dependent relationships are quite similar to those in the strips patterned along the easy axis, as shown in Fig. 3.3. However, the current results seem difficult to be understood, since the effective anisotropy field has no obvious changes in the strips of different widths, as listed in Table 3.1. One thing that can be sure is that the high permeability is mainly contributed by the oscillation of the magnetization in region II (see Fig.3.6), rather than the moments in region I where domains are oriented parallel to the direction of the exciting rf magnetic field. In region II, the complex domains can be subdivided into 180°-wall domain in the center and 90°-wall (or ripple-like) domain at the edge [22, 23]. It is plausible to think that the edge domain can have larger resonance frequency due to the spin pinning effect from the relative "hard" single domain in region I. In narrower strips, the volume ratio of the 90°-wall to 180°-wall domains is expected to increase, thus pushing the averaged spin resonance behavior to a larger frequency.

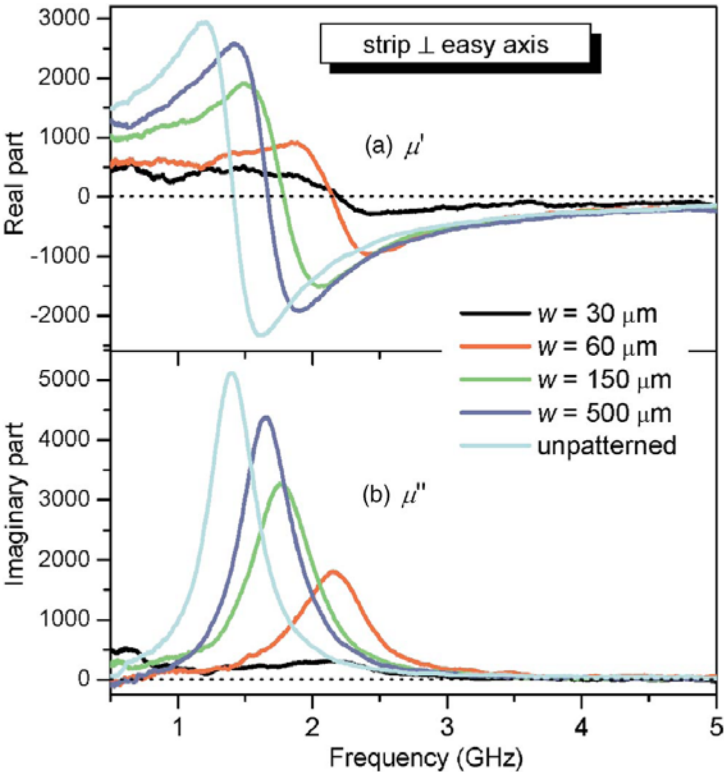

Figure 3.7 (Color online) the real μ' and imaginary parts μ'' of the permeability of the unpatterned film and the strips patterned along the hard axis at widths *w*=30, 60, 150, and 500 μm.

3.2 Strips patterned with different strip width period

In the above part, we found that patterning the magnetic film into strips could improve the magnetic anisotropies and the resonance frequency of the films with dependence on the strip widths and their orientations. In the following, we tried to broaden the width of the resonance absorption peak of the films by constructing composite strip arrays, i.e., one period with multiple strips of different widths. It was motivated by the expectation that each width could contribute to a unique resonance frequency, as shown in Fig. 3.8.

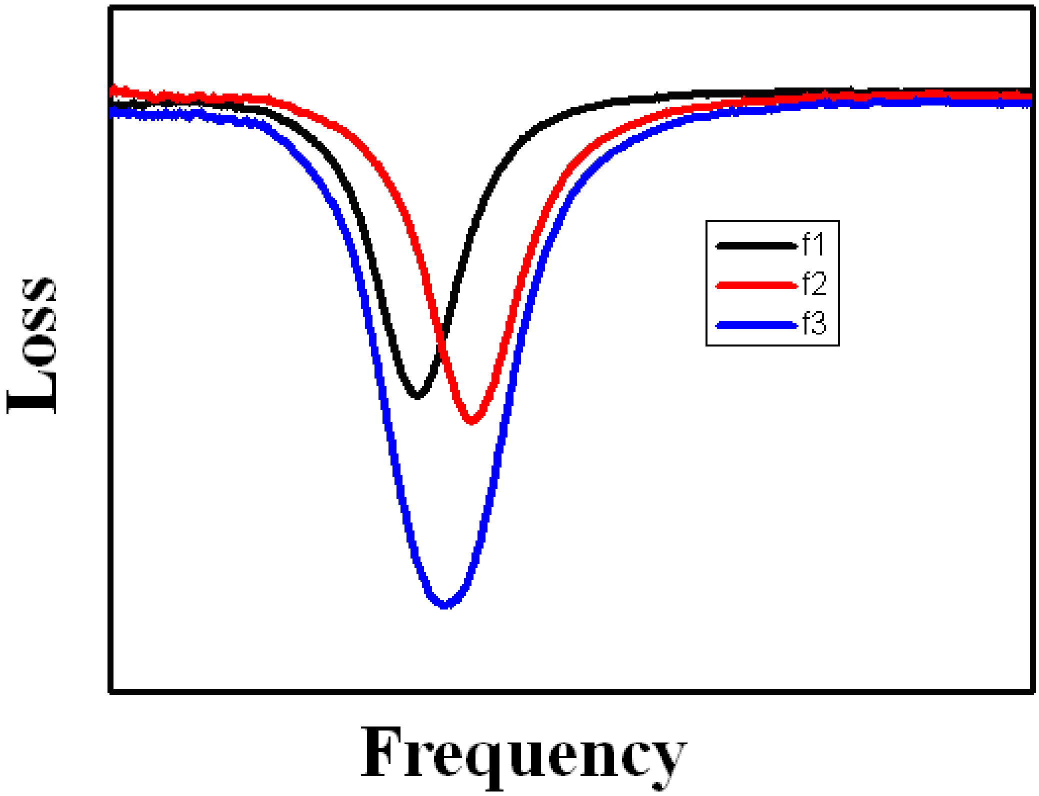

Figure 3.8 Schematic structures of microwave absorption for strips patterned with different strip width structure

Three types of strip samples were fabricated. As schematically shown in Figs. 3.9(a), 3.9(b) and 3.9(c), their basic unit cells had one, two and three strips in different widths, respectively. The selected strip widths (w) were 30, 60, 150, 300 and 500 μm. The gap distance (d) between the adjacent strips was 30 μm. All the strips were patterned along the easy axes of the unpatterned thin films. Their permeability was measured along the hard axes of the unpatterned thin films, which had a uniaxial anisotropy field (H_a) along the easy axis. After patterning, strong demagnetization effect along the strip width would induce an additional shape anisotropy field (H_k^s) along the strip length direction. Thus, the total effective anisotropy field (H_k^{eff}) for the patterned strips would be $H_{ki}^{eff} = H_a + H_{ki}^s$.

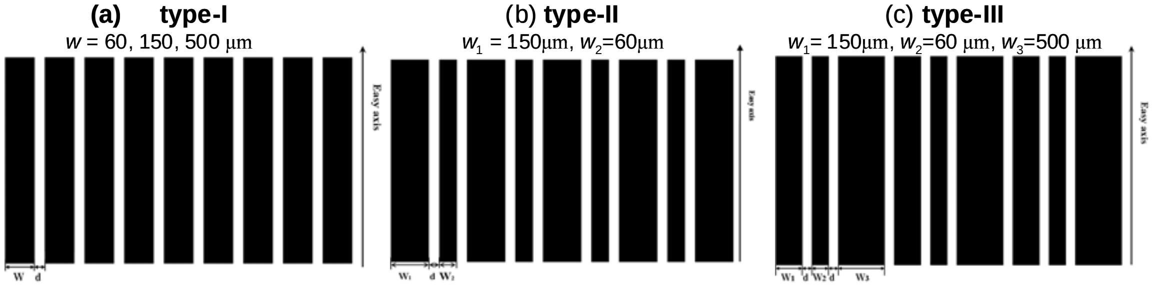

Figure 3.9 Schematic structures of the patterned FeTaN thin films in three types. In (a), all the strips had the same width (w). Here w =30, 60, 150, 300 and 500μm were selected. In (b), one period included two strips of widths = 60 and 150 μm, respectively. In (c), one period included three strips of widths = 60, 150 and 500 μm, respectively. The spacing (d) of the adjacent strips in (a) and (b) and (c) were controlled to be 30 μm, The easy axes of the unpatterned films were along the length directions of the strips.

The FeTaN thin films were deposited on silicon substrates by reactive rf magnetron sputtering. A static magnetic field of about 120 Oe was applied parallel to the substrate surface during deposition in order to induce a uniaxial anisotropy. The thickness of the FeTaN thin films was fixed at 100 nm. Conventional UV photolithography and wet etching were used to make the patterns. The static magnetic property of the thin films was measured using a BH loop tracer. The microwave complex permeability frequency spectra were measured along the hard axis of the thin films.

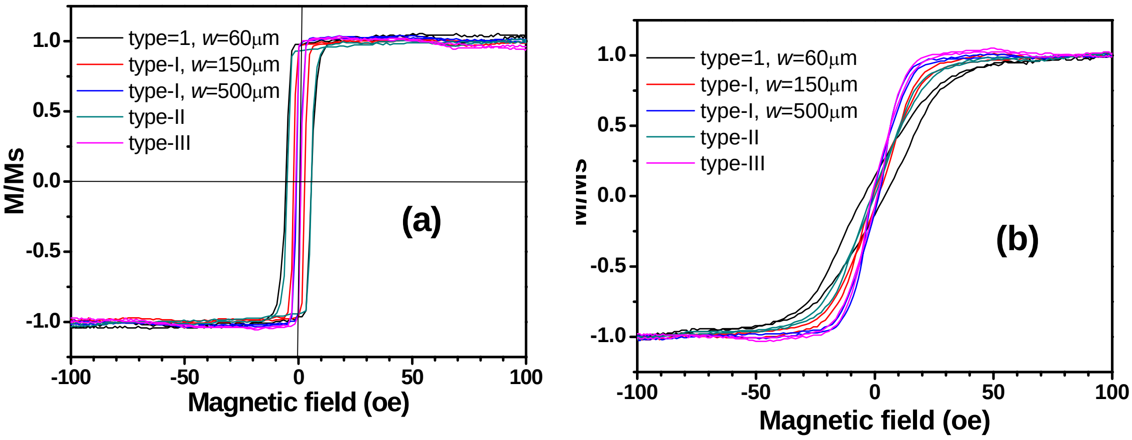

Figure 3.10 (a) Easy and (b) hard-axis hysteresis loops of the patterned strips with the structures given in Figs. 3.9.

Figures 3.10(a) and 3.10(b) show the easy and hard axis hysteresis loops of the patterned strips with the structures given in Figs. 3.9(a)-3.9(c). The hysteresis loops indicate all the patterned samples have well-defined uniaxial anisotropy. The easy-axis magnetization loops show little changes in different patterns. It implies that the domain wall motion for the magnetization reversal was not influenced by the patterning process. This is possible because the strip width is far larger than the domain wall width at least by two orders. For the samples of type-I, their easy-axis coercivities and effective anisotropy fields (estimated from the saturation points of the hard-axis loop) are gradually increased as the strips become narrower, due to the larger shape anisotropy induced in narrower strips formed after patterning. For the samples of type-II and type-III, the values of their coercivities and effective anisotropy fields are in between those of the type-I sample at different widths. This result is understandable because the total anisotropy is proportional to the strip width. In addition, the hysteresis loops show single step domain wall motion or reversal in the three type samples. The magnetostatic interaction between the strips should be strong enough to couple them together. The values of the key magnetic parameters are listed in Table 3.2

.

Pattern (μm)	H_{ce}(Oe)	H_{ch}(Oe)	H_k^{eff}(Oe)	μ’	μ”	f_{FMR} (GHz)	FWHM (GHz)
Type-I (60)	5.7	4.2	35	900	1600	2.17	0.43
Type-I (150)	2.8	～1	21	1300	2300	1.8	0.42
Type-I (500)	1	～1	13.6	1500	2700	1.45	0.39
Type-II	5	～1	22	1100	1800	1.59	0.5
Type-III	1.1	～1	13.7	1300	2100	1.47	0.54

TABLE 3.2 the lists of easy (H_{ce}) and hard-axis (H_{ch}) coercivities, effective

anisotropy field (H_k^{eff}), maximum real (μ') and imaginary (μ'') parts of the permeability, the ferromagnetic resonance frequency (f_{FMR}), and the full width of the resonance peak at the half maximum (FWHM).

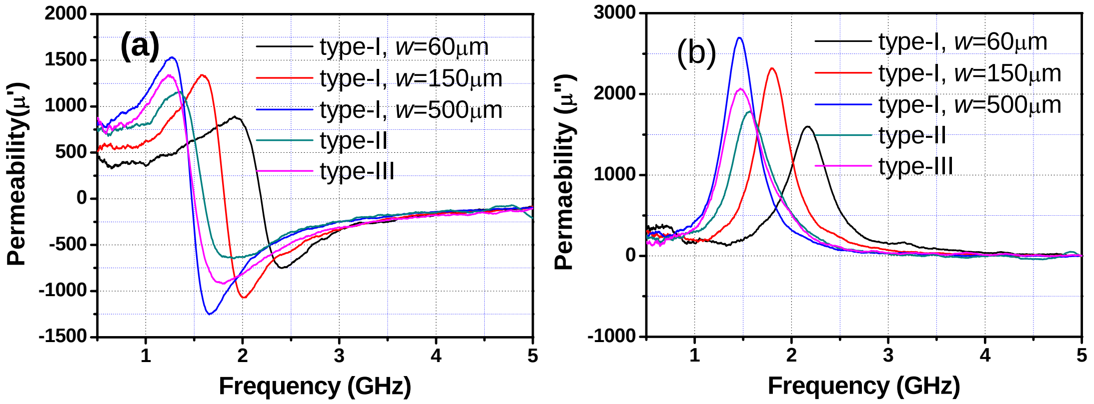

Figure 3.11 (a) Real and (b) imaginary parts of the complex permeability spectra of the FeTaN strips with the structures described in Figs. 3.9(a)-3.9(c)

Figs. 3.11(a) and 3.11(b) show the complex permeability spectra of the three type samples with the structures given in Figs. 3.9. For the sample in type-I, the values of the permeability decrease when the strips become narrower, and the resonance frequency increases. These trends are consistent with the magnetic properties of the strips whose effective anisotropy fields are inversely proportional to the strip width. The reduction of permeability is also partly caused by the fact that the measured permeability is actually an effective permeability calculated using the volume of the unpatterned films without taking the material loss after patterning into account. The f_{FMR} value for the type-I pattern is tuned from 1.5 to 2.2 GHz as the strip width w reduces from 500 to 60 μm. The resonance frequencies for the type-II and III samples are 1.59 and 1.47 GHz, respectively. Compared to the type-I samples, the broadness of the resonance peaks for these two samples have a small increment by

0.1 GHz. It shows the composite strip structure really has the effect in broadening the width of the resonance absorption peak. This effect can be more manifest by further reducing the magnetostatic interaction between the strips. It may be realized by increasing the strip spacing or changing the composition distributions.

In summary, patterning the continuous magnetic film into the strip arrays was proved to be an efficient method to tune the resonance frequency of the film. The broadness of the resonance absorption peak could be further improved by utilizing composite strip structures.

References

[1] M. Yamaguchi, Y. Miyazawa, K. Kaminishi, H. Kikuchi, S. Yabukami, K. I. Arai, and T. Suzuki, J. Magn. Magn. Mater. **268**, 170 (2004).

[2] M. Yamaguchi, K. H. Kim, and S. Ikeda, J. Magn. Magn. Mater. **304**, 208 (2006).

[3] Y. Zhuang, M. Vroubel, B. Rejaei, J. N. Burghartz, and K. Attenborough, J. Appl. Phys. **97**, 10N305 (2005).

[4] Y. Zhuang, B. Rejaei, E. Boellaard, M. Vroubel, and J. N. Burghartz, IEEE Microw. Wirel. Compon. Lett. **12**, 473 (2002).

[5] B. Botters, F. Giesen, J. Podbielski, P. Bach, G. Schmidt, L. W. Molenkamp, and D. Grundler, Appl. Phys. Lett. **89**, 242505 (2006).

[6] Y. Fu, T. Miyo, T. Yamakami, Z. Yang, M. Matsumoto, X. X. Liu, and A. Morisako, IEEE Trans. Magn. **41**, 2905 (2005).

[7] Y. G. Ma, Y. Liu, C. Y. Tan, Z. W. Liu, and C. K. Ong, J. Appl. Phys. **100**, 054307 (2006).

[8] Y. G. Ma and C. K. Ong, J. Phys. D: Appl. Phys. **40**, 3286 (2007).

[9] H. Greve, C. Pochstein, H. Takele, V. Zaporojtchenko, F. Faupel, A. Gerber, M. Frommberger, and E. Quandt, Appl. Phys. Lett. **89**, 242501 (2006).

[10] M. Vroubel, Y. Zhuang, B. Rejaei, and J. Burghartz, J. Magn. Magn. Mater. **258**, 167 (2003).

[11] Z. W. Liu, Y. Liu, C. Y. Tan, L. Yan, and C. K. Ong, J. Appl. Phys. **99**, 043903 (2006).

[12] Z. W. Liu, C. Y. Tan, Y. Liu, and C. K. Ong, J. Appl. Phys. **101**, 023912 (2007).

[13] Y. G. Ma, X. H. Li, T. Xie, F. L. Wei, and Z. Yang, Mater. Sci. Eng., B **103**, 233 (2003).

[14] G. G. Wu, D. P. Wu, K. H. Zheng, F. L. Wei, Z. Yang, and A. S. Kamzin, Chin. Phys. **14**, 1238 (2005).

[15] F. Johnson, C. Y. Um, M. E. McHenry, and H. Garmestani, J. Magn. Magn. Mater. **292**, 93 (2006).

[16] Y. Shimada, M. Yamaguchi, S. Ohnuma, T. Itoh, W. D. Li, S. Ikeda, K. H. Kim, and H. Nagura, IEEE Trans. Magn. **39**, 3052 (2003).

[17] M. Vroubel, Y. Zhuang, B. Rejaei, J. N. Burghartz, A. M. Crawford, and S. X. Wang, IEEE Trans. Magn. **40**, 2835 (2004).

[18] S. Ikeda, T. Nagae, Y. Shimada, K. H. Kim, and M. Yamaguchi, J. Appl. Phys. **99**, 08P507 (2006).

[19] Y. Zhuang, M. Vroubel, B. Rejaei, J. N. Burghartz, and K. Attenborough, J. Appl. Phys. **99**, 08C705 (2006).

[20] G. Perrin, J. C. Peuzin, and O. Archer, J. Appl. Phys. **81**, 5166 (1997).

[21] C. Kittel, Phys. Rev. **73**, 155 (1948).

[22] U. Memmert, P. Leinenbach, J. Losch, and U. Hartmann, J. Magn. Magn. Mater. **190**, 124 (1998).

[23] F. Schoenstein, P. Aublanc, H. Pages, S. Queste, V. Barentin, A. Adenot, N. Mallejac, and O. Acher, J. Magn. Magn. Mater. **292**, 201 (2005).

Chapter 4

MICROWAVE MEASUREMENT FOR EM ABSORBER

4.1 FeTaN lamination stack for EM absorber application

In this chapter, we will discuss the microwave properties of FeTaN lamination stack. The quantities μ_{eff} and ε_{eff} are relative permittivity and permeability of the stack. The relationships of the effective permittivity and permeability of the stack are given by a simple Wiener's law as following [1]:

$$\mu_{eff} = \mu_{stack} \tag{4.1}$$

$$\varepsilon_{eff} = \frac{\varepsilon_d}{1-q} \tag{4.2}$$

Where ε_d is the effective permittivity of the nonmagnetic dielectric materials, and q are the volume fraction of ferromagnetic in the FeTaN lamination stack.

For single 100-nm FeTaN film grown on 8-μm Mylar substrate, ε_{eff} (about 3.4 for Mylar substrate) is larger than μ_{eff} (about 1.25% of FeTaN film permeability value). To improve the effective permeability of FeTaN lamination stack, we need to increase the amount of FeTaN films in stack. For single layer FeTaN films, good soft magnetic properties were obtained only when they had the thicknesses of tens of nanometers. But in thick films (thickness>100 nm), the soft magnetism was seriously degraded by the excess grain growth. Laminating the FeTaN layers with Al_2O_3 spacers can control the film growth, and obtain good soft magnetic properties in thick films [2]. Therefore, the FeTaN films and Al_2O_3 interlayers were deposited on both sides of a 8-μm polyethylene terephthate (Mylar) substrate to form a unit of FeTaN lamination stack by RF magnetron sputtering. The structure of one unit is shown in Fig.4.1. On each side of the Mylar substrate, three 100-nm FeTaN layers are laminated with two 8-nm Al_2O_3 layers. Here, the 6 layers of FeTaN are used to increase its volume fraction in the unit, and Al_2O_3 interlayers were deposited to prevent the deterioration of the soft magnetic properties. To make the stack, 54 FeTaN film units were glued together using epoxy to form a rectangular laminate stack suitable for the microstrip measurement method. The dimension of the stack is $11 \times 22 \times 1.25$ mm^3 (width × length × thickness). The volume fractions of FeTaN and Al_2O_3 layers in the stack are estimated to be about 2.1% and 0.1%, respectively. The static magnetic properties were measured with a low-field *M-H* tracer.

Figure 4.1 Structure of one unit of FeTaN lamination stack

For the deposition of the FeTaN film, a 3-inch iron disc covered with tantalum chips (6% surface area) was used as the sputtering target. Before sputtering, the chamber was pumped down to a base pressure of 3×10^{-7} Torr. During sputtering, the chamber pressure was raised to 7×10^{-4} Torr by introducing a gas mixture consisting of nitrogen (3%) and argon at a flow rate of 16 sccm (sccm denotes cubic centimeter per minute at STP). RF power was kept at 80 W. A magnetic field of 140 Oe was applied parallel to the substrate surface during sputtering to induce an in-plane uniaxial magnetic anisotropy. For the sputtering of Al_2O_3 layers, a 2-inch Al_2O_3 target and pure argon were used.

4.2 Introductions to transmission line

A transmission line is a system of conductors having a precise geometry and arrangement which is used to transfer power from source to load with minimum loss. All transmission lines have a characteristic impedance value which is typically constant.

There are a few type of transmission line, namely, parallel-wire, coaxial cable, microstrip and waveguide as shown in Fig. 4.2 [3]. The parrel-wire transmission line consist of two conductors spaced a certain distance apart as shown in Fig. 4.2, and is mainly used for low frequencies. At high frequencies (above 200MHz), serious losses occur due to radiation from the surface and the skin effect. The simplest form of a stripline is a pair of parallel plates of finite width. This is a modification of the model of infinitely wide plates, resulting in a distortion of the field patterns with some field fringing into the space outside the line. However, if the spacing between the plates in made very small compared with the wavelength, then the radiation is small and a low loss transmission lines which can take the form of a flattened coaxial line, referred to as embedded stripline. It is formed by sandwiching a conductor between two conducting ground plates insulated by dielectric and is used for unbalanced system.

A waveguide is a hollow metal tube used for transmitting electromagnetic waves. Waveguides only propagate signals with a frequency above a given cut-off, which is determined by the width of the waveguide.

The coaxial lines consist of two conductors. The inner conductor is insulated from and surrounded by the outer conductor (called the shield) and centered precisely by means of a supporting dielectric material, forming the coaxial line. Coaxial lines overcome the radiation loss problems due to the shielding provided by the outer conductor surrounding the center conductor.

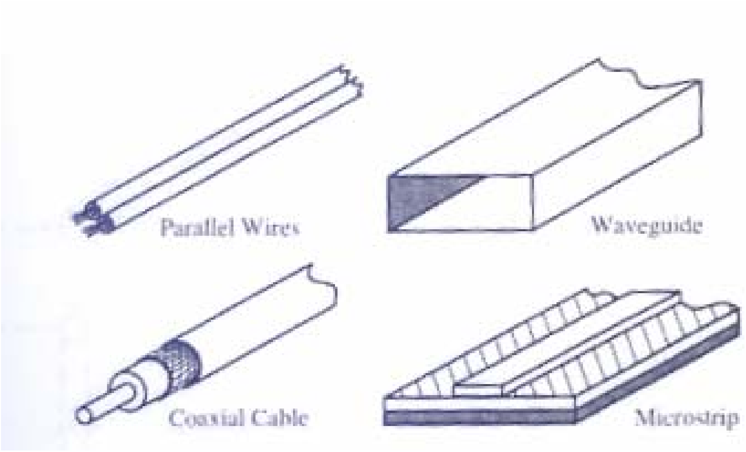

Figure 4.2 Type of transmission line [3]

4.2.1 Transmission line theory

In this section, the properties of transmission line will first be derived in terms of relatively low-frequency currents and potential differences. The radiation effect is neglected. A small element of length Δz of a two wire transmission line is considered as shown in Fig.4.3 [4].

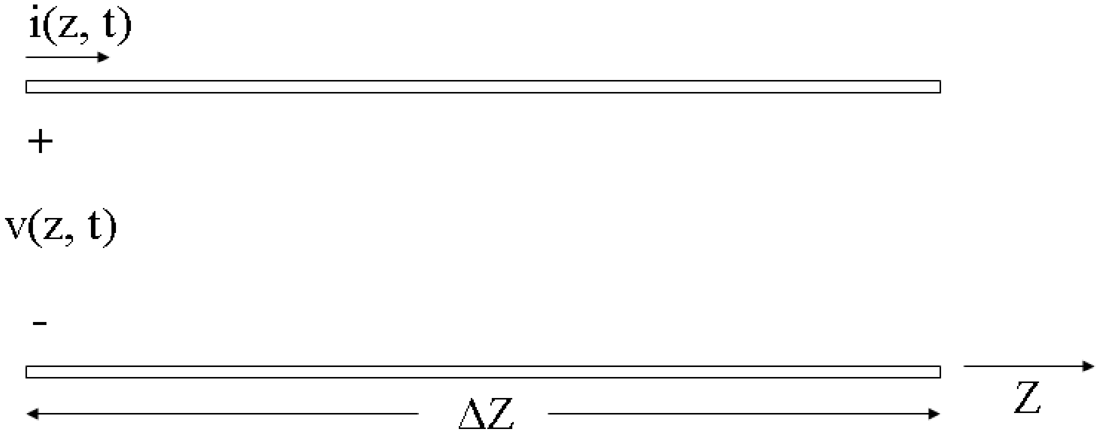

Figure 4.3. Voltage and current definitions for an incremental length of transmission line

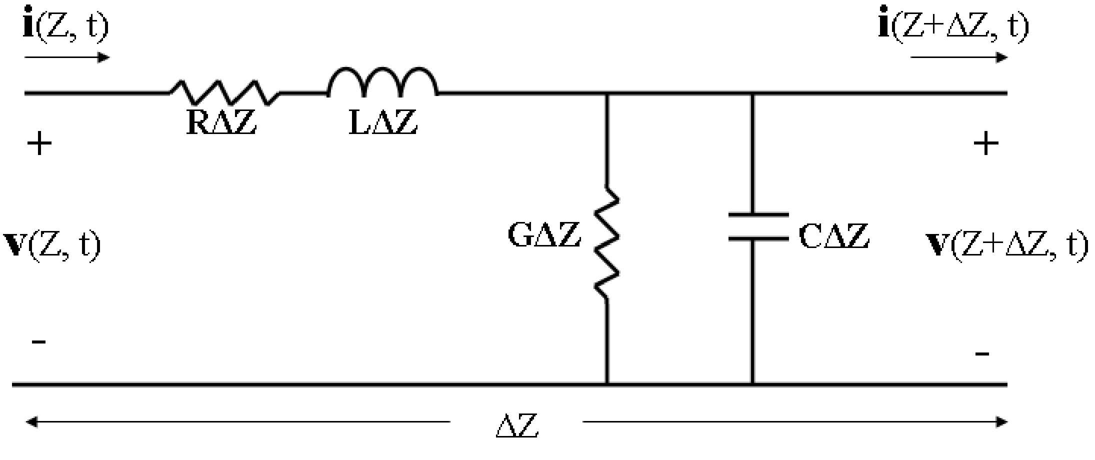

Figure 4.4 the Lumped-element circuit mode for a transmission line

Transmission line is often schematically represented as a two-wire line. The current flowing in the line and the potential difference between the wires of the line are functions of distance along the line, which will be defined in the direction z. The piece of line of infinitesimal length of Fig 4.3 can be modeled as a lumped element circuit, as shown R, L, G, C are per unit length quantities defined as follows:

R = series resistance per unit length, for both conductors, in Ω/m.

L = series inductance per unit length, for both conductors, in H/m.

G = shunt conductance per unit length, in S/m.

C = shunt capacitance per unit length

L represents the total self-inductance of the two conductors, and C is due to the close proximity of the two conductors. R represents the resistance due to the finite conductivity of the conductors, and G is due to dielectric loss in the material between the conductors. Therefore, R and G represent loss. A finite length of transmission line can be viewed as a cascade of sections of the form shown in Fig. 4.4

From the circuit of Fig.4.3, Kirchhoff's law can be applied to give

$$v(z,t) - R\Delta z i(z,t) - L\Delta z \frac{\partial i(z,t)}{\partial t} - v(z+\Delta z,t) = 0 \tag{4.3}$$

$$i(z,t) - R\Delta z v(z,t) - C\Delta z \frac{\partial v(z+\Delta z,t)}{\partial t} - i(z+\Delta z,t) = 0 \tag{4.4}$$

Dividing and by Δz and taking the limit as Δz→0, gives the following different equations:

$$\frac{\partial i(z,t)}{\partial z} = -Gv(z,t) - C\frac{\partial v(z,t)}{\partial t} \tag{4.5}$$

$$\frac{\partial v(z,t)}{\partial z} = -Ri(z,t) - L\frac{\partial i(z,t)}{\partial t} \tag{4.6}$$

These equations are the time-domain form of the transmission line equation.

For the sinusoidal steady-state condition, with cosine-based phases, Eq. 4.5 and Eq. 4.6 simplify to

$$\frac{dI(z)}{dz} = -(G + j\omega C)V(z) \tag{4.7}$$

$$\frac{dV(z)}{dz} = -(R + j\omega L)I(z) \tag{4.8}$$

The two equations of can be solved simultaneously to give wave equation for V(z) and I(z):

$$\frac{d^2 I(z)}{d^2 z} - \gamma^2 I(z) = 0 \tag{4.9}$$

$$\frac{d^2 v(z)}{d^2 z} - \gamma^2 v(z) = 0 \tag{4.10}$$

Where $\gamma = \alpha + j\beta = \sqrt{(R + j\omega L)(G + j\omega C)}$, γ is the complex propagation constant, which is a function of frequency. Therefore, traveling wave solution to can be found as

$$V(z) = V_0^+ e^{-\gamma z} + V_0^- e^{\gamma z} \tag{4.11}$$

$$I(z) = I_0^+ e^{-\gamma z} + I_0^- e^{\gamma z} \tag{4.12}$$

Where the $e^{-\gamma z}$ term represents wave propagation in the +z direction, and the $e^{\gamma z}$ term represents wave propagation in the –z direction. Furthermore,

$$e^{-\gamma z} = e^{-\alpha} e^{-j\beta z} \tag{4.13}$$

α determines the attenuation along the line in the +z direction, and β determines the phase shift along the line in the +z direction.

Applying the voltage with cosine-based phase to Eq. 4.11 gives the current on the line:

$$I(z) = \frac{\gamma}{R + j\omega L}[V_0^+ e^{-\gamma z} - V_0^- e^{\gamma z}] \tag{4.14}$$

Comparison with Eq. 4.12 shows that characteristic impedance, Z_0, can be defined as

$$Z_0 = \frac{R + j\omega L}{\gamma} = \sqrt{\frac{R + j\omega L}{G + j\omega C}} \tag{4.15}$$

To relate the voltage and current on the line as

$$\frac{V_0^+}{I_0^+} = Z_0 = -\frac{V_0^-}{I_0^-} \tag{4.16}$$

Then can be rewritten in the following form:

$$I_z = \frac{V_0^+}{Z_0} e^{-\gamma z} - \frac{V_0^-}{Z_0} e^{\gamma z} \tag{4.17}$$

$$V_{(z,t)} = \left|V_0^+\right| \cos(wt - \beta z + \phi^+) e^{-\alpha z} + \left|V_0^-\right| \cos(wt + \beta z + \phi^-) e^{\alpha z} \tag{4.18}$$

For lossless transmission lines, the distributed conductor resistance *R* and dielectric conductance *G* are both zero. In this case the characteristic impedance is real and is equal to:

$$Z_0 = \sqrt{\frac{L}{C}} \tag{4.19}$$

The propagation constant γ is also imaginary with:

$$\alpha = 0 \tag{4.20}$$

$$\gamma = j\beta = j\omega\sqrt{LC} \tag{4.21}$$

Expressing the waves in time-domain,

$$v(t,z) = \left|V^+\right| \cos(\omega t - \beta z) + \left|V^-\right| \cos(\omega t + \beta z) \tag{4.22}$$

$$i(t,z) = \frac{\left|V^+\right|}{Z_0} \cos(\omega t - \beta z) + \frac{\left|V^-\right|}{Z_0} \cos(\omega t + \beta z) \tag{4.23}$$

In any transmission line, the phase velocity Vp

$$v_P = \frac{\omega}{\beta}, \text{ where } \beta = \frac{2\pi}{\lambda} \tag{4.24}$$

In lossless transmission line, $\beta = \omega\sqrt{LC}$

Therefore $v_P = \frac{\omega}{\beta} = \frac{1}{\sqrt{LC}}$ (4.25)

A lossless transmission line is preferred but not possible in practice. The losses are mainly contributed by imperfection of transmission line dimension, radiation loss, dielectric loss and magnetic loss, etc [5].

4.2.2 Mircrostrip transmission line measurement method

In this section, we will discuss the microwave transmission line measurement methods for characterization of magnetic materials. Non-resonant methods based on transmission line method are employed to get complex permittivity and permeability of sample. Non-resonant methods are classified as reflection and transmission line methods. We only study the non-resonant methods.

4.2.2.1 Reflection method

4.2.2.1.1 Perturbation method

Perturbation method has been developed by Liu Yan etc. in our lab [4]. In the configuration shown in Fig. 4.5, the shorted transmission line consists of two portions: the empty portion without thin film and the sample portion which is loaded with the sample under study. The effective permittivity of the transmission line can be obtained from the reflection coefficient measured at starting point of the transmission line:

$$s_{11} = -e^{-2(\gamma_1 l_{emp} + \gamma_2 l_{sample})} \tag{4.26}$$

$$\gamma = j\frac{\omega}{c_0}\sqrt{\varepsilon_{eff}\mu_{eff}} \tag{4.27}$$

Where S_{11} is the reflection coefficient with or without sample insertion, l_{empty} is the length of the empty portion, l_{sample} is the length of the sample portion, and f is the measurement frequency. γ_1 and γ_2 is the propagation constant in empty portion and sample portion, respectively.

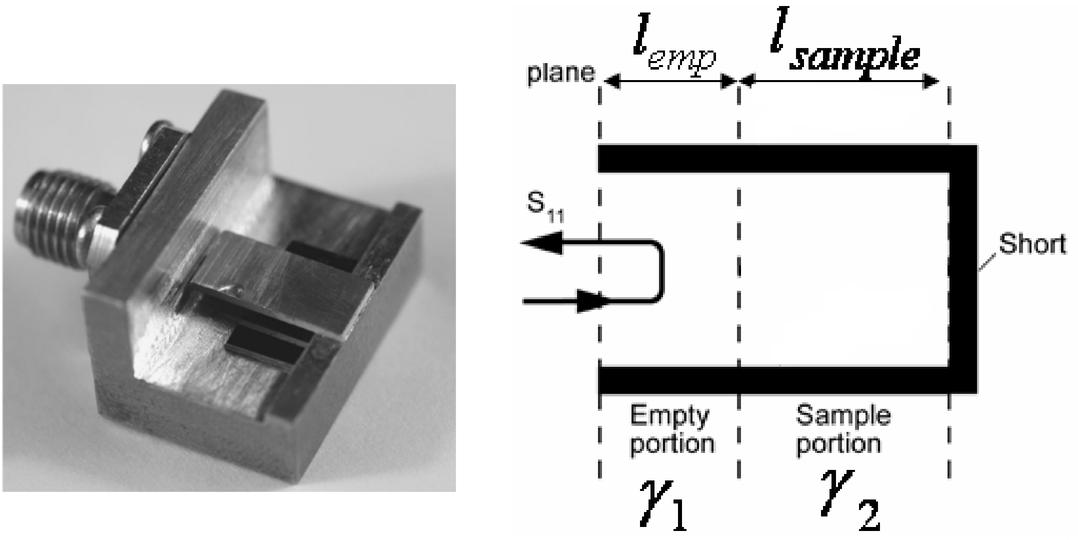

Figure 4.5 Microstrip circuits for characterization of magnetic thin films.

Before the thin sample is inserted, γ_1 and γ_2 is determined by:

$$\gamma_1 = \gamma_2 = j\frac{2\pi f}{c_0}\sqrt{\varepsilon_{eff}^{emp}} \tag{4.28}$$

Where ε_{eff}^{emp} is the effective permittivity of transmission line of empty portion. The reflection coefficient s_{11}^{emp} is:

$$s_{11}^{emp} = -e^{-\frac{4\pi f}{c_0}\sqrt{\varepsilon_{eff}^{emp}}(l_{air}+l_{sample})} \tag{4.29}$$

After only insertion of substrate, the sample portion of propagation constant γ_3 changes to:

$$\gamma_3 = j\frac{2\pi f}{c_0}\sqrt{\varepsilon_{eff}^{sub}} \tag{4.30}$$

Where ε_{eff}^{sub} is the effective permittivity of transmission line of sample portion. The reflection coefficient s_{11}^{sub} is:

$$s_{11}^{sub} = -e^{-\frac{4\pi f}{c_0}\sqrt{\varepsilon_{eff}^{emp}}l_{emp}-\frac{4\pi f}{c_0}\sqrt{\varepsilon_{eff}^{sub}}l_{sample}} \tag{4.31}$$

After insertion of substrate and magnetic film, by assuming that the effective permittivity of the transmission line does not change, the effective permeability of the perturbed transmission line is given by

$$\gamma_2 = j\frac{2\pi f}{c_0}\sqrt{\varepsilon_{eff}^{sub}\mu_{eff}} \tag{4.32}$$

The reflection coefficient s_{11}^{sample} is:

$$s_{11}^{sample} = -e^{-\frac{4\pi f}{c_0}\sqrt{\varepsilon_{eff}^{emp}}l_{emp}-\frac{4\pi f}{c_0}\sqrt{\varepsilon_{eff}^{sub}\mu_{eff}}l_{sample}} \tag{4.33}$$

As the change of the effective permeability of the transmission line from unity to the value given by Eq. 4.33 is due to the magnetic properties of the thin film, the complex permeability of the thin film can be obtained from the change of effective permeability of the transmission line

$$\mu_{film}(f) = \frac{K}{t}[\mu_{eff}(f)-1] \tag{4.34}$$

Where t is the thickness of the thin film under test, and K is the scaling coefficient of the shorted transmission line, which is determined by the structure of the shorted transmission line and is independent of the thin film under test. The scaling coefficient K can be obtained by calibrating the shorted transmission line with a standard sample whose permeability is known, or by adjusting the real part of the complex permeability at low frequency to fit the value of initial permeability determined by

$$\mu'_{\text{int}ial} = \frac{M_s}{H_a} + 1 \qquad (4.35)$$

Where Ms is the saturation magnetization and Ha is the anisotropic field of the magnetic thin film under test. Once the scaling coefficient K is determined, it can be used for other samples.

4.2.2.1.2 Shorted transmission line method

i. Measurement principle

To measure the microwave properties of stack, a measurement cell was designed, as shown in Fig. 4.6. The electric and magnetic distribution in the cell was shown in Fig 4.7. Because the imperfection of the measurement line is mainly from the coaxial-to-strip junction, the cell was designed including two portions, the low permittivity (relative permittivity ε_r = 2.94 - 0.0012j at 10 GHz, made by Rogers 6002 PCB board) portion and the empty portion for sample loading. The low permittivity portion has a characteristic impedance of 50 Ω calculated by HFSS software. The cell dimensions are marked in Fig. 4.6(b), w=3.9 mm, d=13 mm, l=11 mm, and the height of the cell is 1.25 mm. The S-parameter measurement was performed with a

HP8722D network analyzer from 0.5 to 3.5 GHz. The TRL (Thru, Reflect, Line) calibration was realized with the standard calibration kits to compensate the errors due to S-parameter test set and cables. The appendix A descript this calibration process in details.

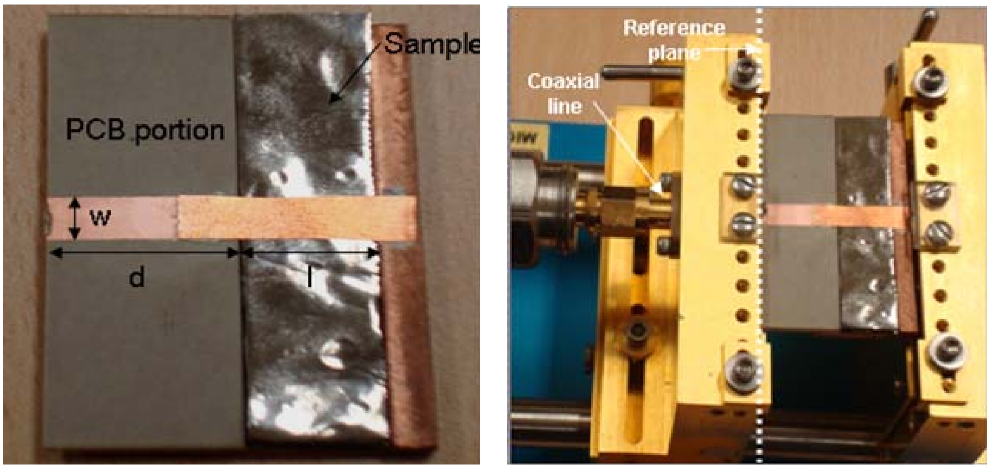

Figure 4.6 Fixture of measurement cell

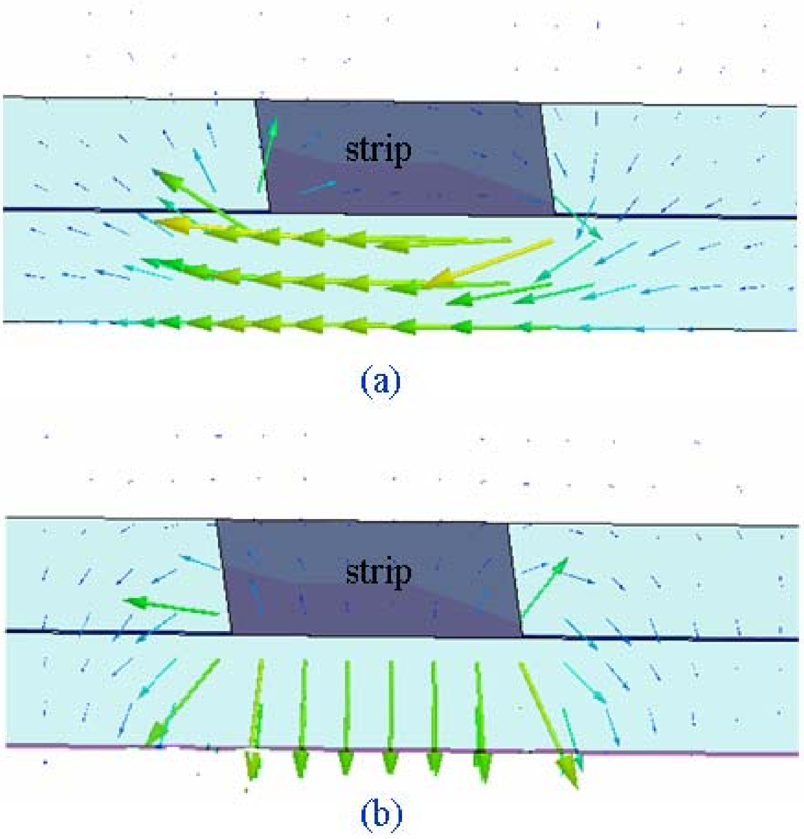

Figure 4.7 Magnetic field (a) and electric field (b) distribution at the cross section of the cell

It should be noted that in the cell only quasi-transverse electromagnetic (TEM) mode propagates along the transmission line at low microwave frequencies. The characteristic parameters for deriving materials' properties mainly include characteristic impedance Z, propagation constant γ, effective permittivity $\varepsilon_{\mathrm{eff}}$, and effective permeability μ_{eff}. These parameters are related by the following equations:

$$Z = Z_0 \sqrt{\frac{\mu_{eff}}{\varepsilon_{eff}}} \tag{4.36}$$

$$\gamma = j\frac{\omega}{c_0}\sqrt{\mu_{eff}\varepsilon_{eff}} \tag{4.37}$$

Where Z_0 is the characteristic impedance of the microstrip line without substrate (with air), c_0 is the light speed in free space, and ω is the angular frequency.

The cell was regarded as a shorted load transmission line, as sketched in Fig. 4.8. The relationship between reflection parameter S_{11} (measured at coaxial-to-strip junction) and reflection coefficient Γ (at interface between low permittivity portion and empty portion due to impedance mismatch) is given by [4]:

$$S_{11}^{air} = e^{-2\gamma d}\Gamma_{air} \tag{4.38}$$

$$S_{11}^{stack} = e^{-2\gamma d}\Gamma_{stack} \tag{4.39}$$

Where S_{11}^{air} and S_{11}^{stack} are the reflection parameter with or without stack, Γ_{air} and Γ_{stack} is the reflection coefficient with or without stack, and γ is the propagation constant of the low permittivity portion and its value is mainly affected by the dielectric and metallic losses of low permittivity portion.

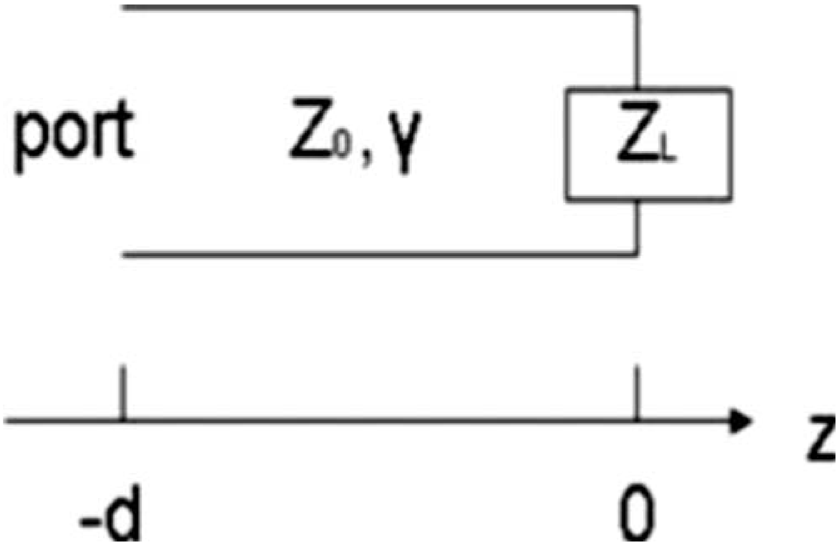

Figure 4.8 Transmission line terminated by a shorted load of impedance Z_L.

According to Fresnel's rule [7], reflection coefficient Γ at interface between low permittivity portion and empty portion is given by:

$$\Gamma = \frac{Z_L - Z_{pcb}}{Z_L + Z_{pcb}} \tag{4.40}$$

Where Z_{pcb} is the impedance of low permittivity portion and Z_L is the input impedance of the shorted transmission line, empty portion (with or without sample).

They can be expressed as:

$$Z_{load} = Z_0 \sqrt{\mu'} / \sqrt{\varepsilon'} \tag{4.41}$$

$$Z_L = Z_{load} \tanh(\gamma' l) \tag{4.42}$$

$$Z_{load} = Z_0 \sqrt{\mu'} / \sqrt{\varepsilon'} \tag{4.43}$$

Where ε_{pcb} is the relative permittivity of Rogers 6002 PCB board, Z_{load} is the impedance of empty portion, μ′ and ε′ are the effective permeability and permittivity of material in empty portion, γ′ is the propagation constant of the empty portion. It can be derived from Eqs. (4.26) to (4.33) that

$$\sqrt{\frac{\mu_{eff}}{\varepsilon_{eff}}}\tanh\left(\frac{2\pi i l}{\lambda}\sqrt{\mu_{eff}\varepsilon_{eff}}\right)=\frac{\left(\frac{S_{11}^{stack}}{S_{11}^{air}}\times\Gamma_{air}+1\right)\sqrt{\frac{1}{\varepsilon_{pcb}}}}{1-\frac{S_{11}^{stack}}{S_{11}^{air}}\Gamma_{air}} \tag{4.44}$$

For our FeTaN lamination stack, though the permittivity of Al_2O_3 crystalline (about 10) is larger than Mylar (about 3.4), Mylar substrate (8μm) is almost 250 times the thickness of 4 Al_2O_3 layers in one unit of FeTaN lamination stack. Thus ε_{eff} is almost the same as the Mylar substrate permittivity, which equals to 3.4 - j0.034 at low frequency. Furthermore, we also insert another FeTaN multilayer sample (similar structure with the sample in this paper) into 7-mm coaxial line to get its permittivity and permeability. The complex permittivity of sample is about (4±0.2) - 0.1j at low frequencies, which is near the permittivity of Mylar substrate.

Therefore, μ_{eff} can be determined from S_{11}^{air} and S_{11}^{stack} using Eqs. (4.44). However, the propagation mode in the microstrip line cell is not a strict TEM mode, thus a full wave electromagnetic analysis is needed to determine the accurate value of μ_{eff}. For this purpose, the S-parameter measurement needs a microstrip line cell electromagnetic analysis (direct problem) combined with an optimization process (inverse problem) [4, 8-10]. HFSS software was employed to electromagnetic analysis and optimization procedure. μ_{eff} was used in the simulation as the initial value. The optimized effective permeability value is valid only when calculated and measured values of the S_{11} are reasonable close, $\left|S_{11}^{cal}-S_{11}^{mea}\right|<0.1\,\mathrm{dB}$, where S_{11}^{cal} is obtained by HFSS simulation and S_{11}^{mea} is the experiment result.

ii Experiment results

Figure 4.9 shows the easy and hard axis hysteresis loops of the FeTaN lamination stack. For a single-layered FeTaN film grown on Mylar substrate, the hysteresis loops show a strong uniaxial anisotropy, as shown in the inset of Fig. 4.9. However, FeTaN lamination stack is almost isotropic. Such an apparent change in anisotropy might be ascribed to several possible reasons. First, the angle distribution of the easy-axis direction of each FeTaN layer is inevitable after stacking [11]. Second, the interaction between FeTaN layers will affect the alignment of magnetic moments. Third, the stress induced by gluing process in the stack will have in-negligible influences on the soft magnetic properties [1].

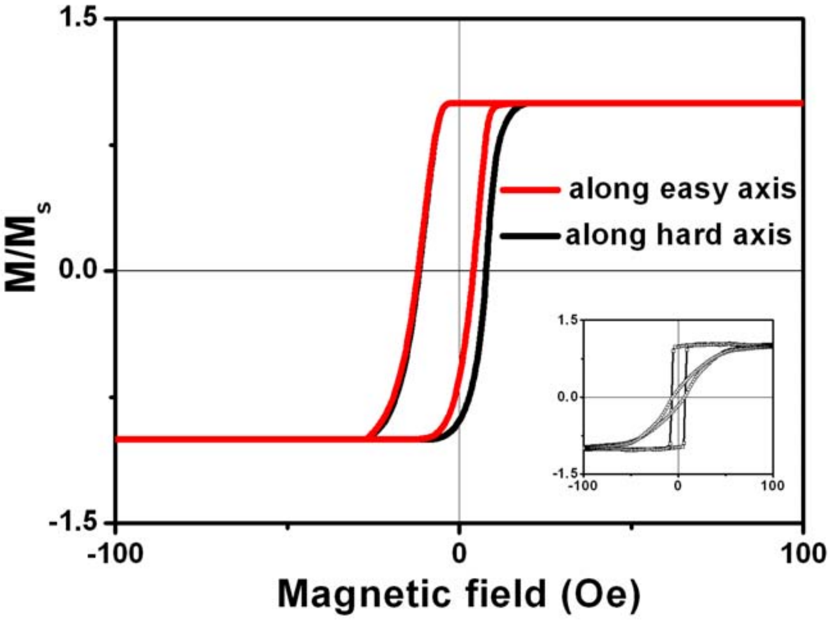

Figure 4.9 (Color line) Hysteresis loops of FeTaN lamination stack and single FeTaN layer (inset)

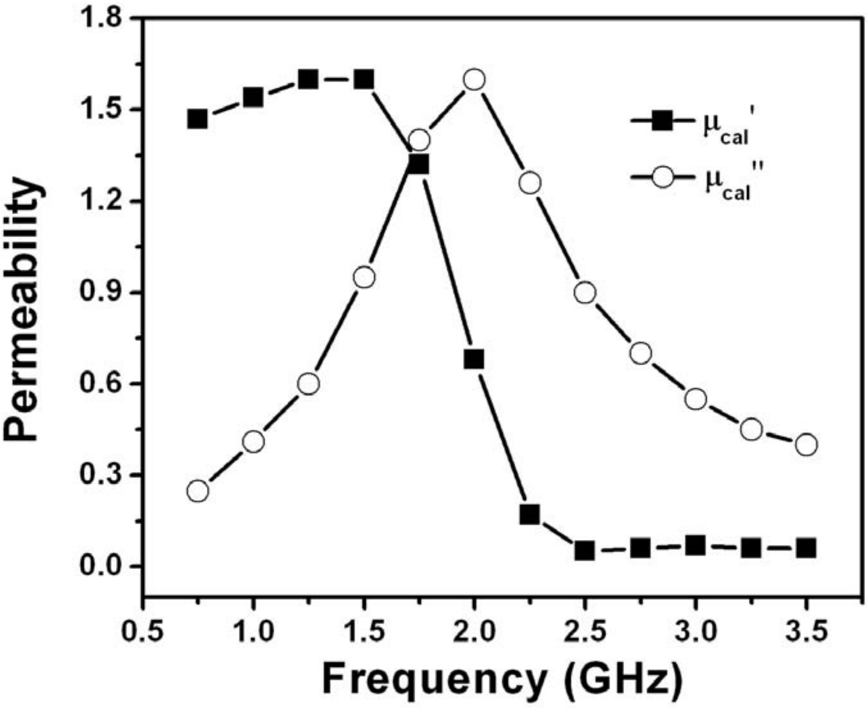

Figure 4.10 Real (μ') and imaginary permeability spectra (μ'') of the FeTaN lamination stack with Eqs. (4.34)

Figure 4.10 shows the real (μ') and imaginary permeability spectra (μ'') of the FeTaN lamination stack, calculated from measured *S*-parameters. High resonance frequency f_r around 2 GHz with effective μ' of 1.6 at $f < f_r$, and μ'' of 1.7 at f_r can be observed. The measurement was performed without any applied external magnetic field. Therefore, this natural resonance frequency, which is due to the precession of magnetic moments around the easy axis, indicates the magnetic anisotropy of each FeTaN layer, though for the whole stack, the magnetic anisotropy is not obvious as shown in Fig. 4.9.

The above effective permeability value for optimization is made in two steps. The first step is simulating the imperfection of the whole microstrip cell with HFSS software, since the measured S_{11} value is affected by the whole microstrip cell losses (dielectric, metallic and radiation) [5]. The second step is minimizing the difference of calculated S_{11} values by HFSS software and measured S_{11} values for FeTaN lamination stack. At first step, we simulate the conditions before sample inserted into the cell, where air ($\varepsilon=\mu=1$) is regarded as a calibration standard for our microstrip cell. By assuming all the differences between calculated and measured S_{11} values are only due to the imperfection of transmission line in low loss dielectric material (Rogers 6002 PCB board) loss portion, the effective ε'' value of Rogers 6002 PCB board was adjusted to reduce these difference before $\left|S_{11}^{\mathrm{cal}} - S_{11}^{\mathrm{mea}}\right| < 0.1\,\mathrm{dB}$ was achieved. Then, we set this optimum ε'' value as a standard Rogers 6002 PCB board parameter, and use these parameters to calculate the S_{11} value of FeTaN lamination stack at second step.

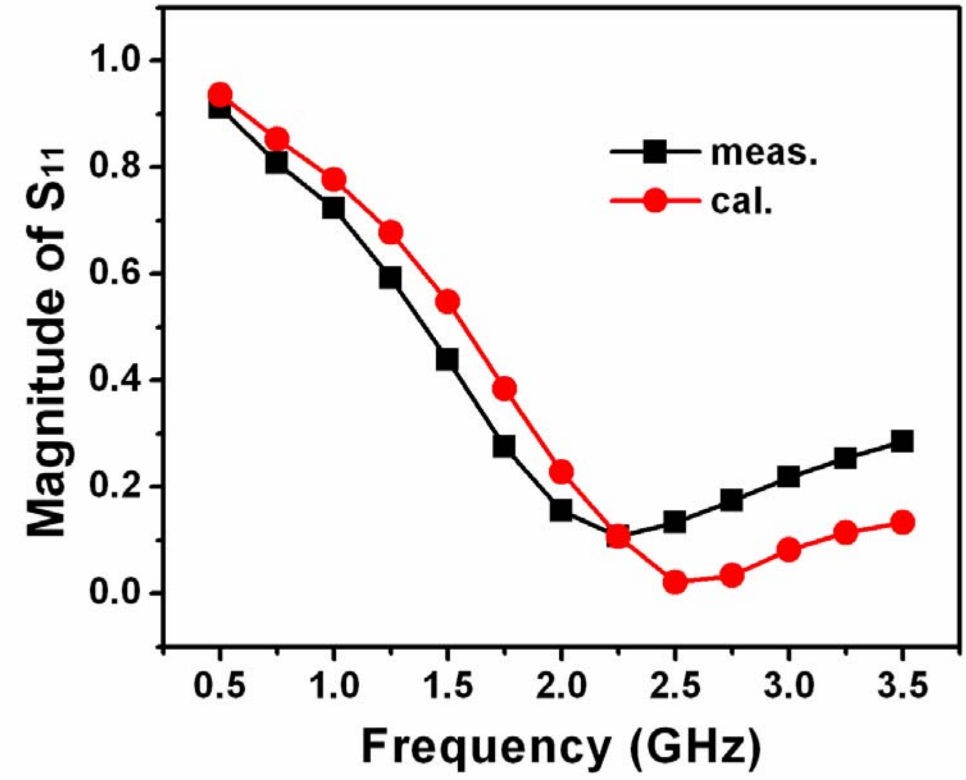

Figure 4.11 Frequency dependence of magnitude of calculated and measured S_{11}

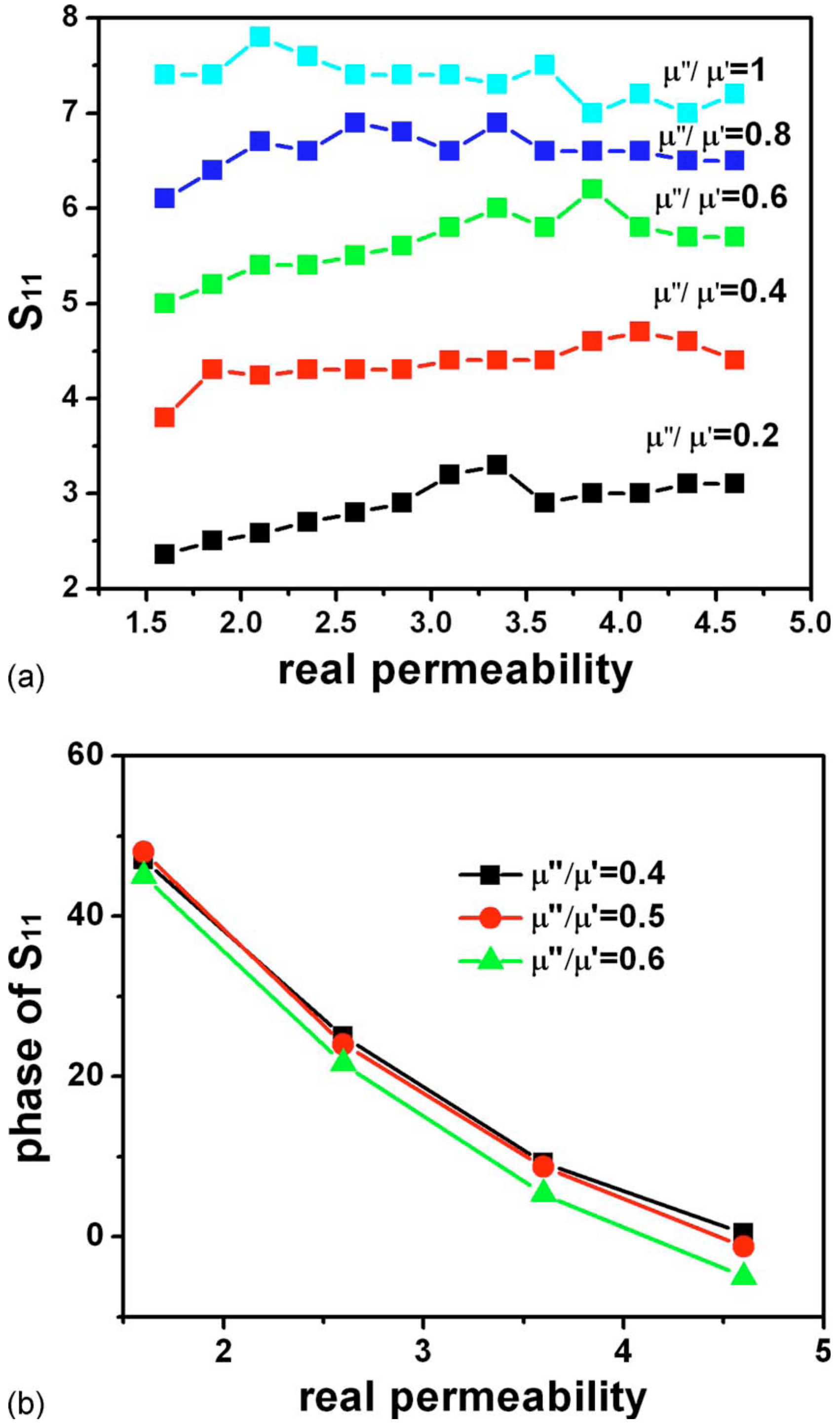

Figure 4.12 (Color online) (a) Real permeability and (b) magnetic loss tangent dependence of S_{11} and phase of S_{11} at 1.25 GHz for FeTaN lamination stack.

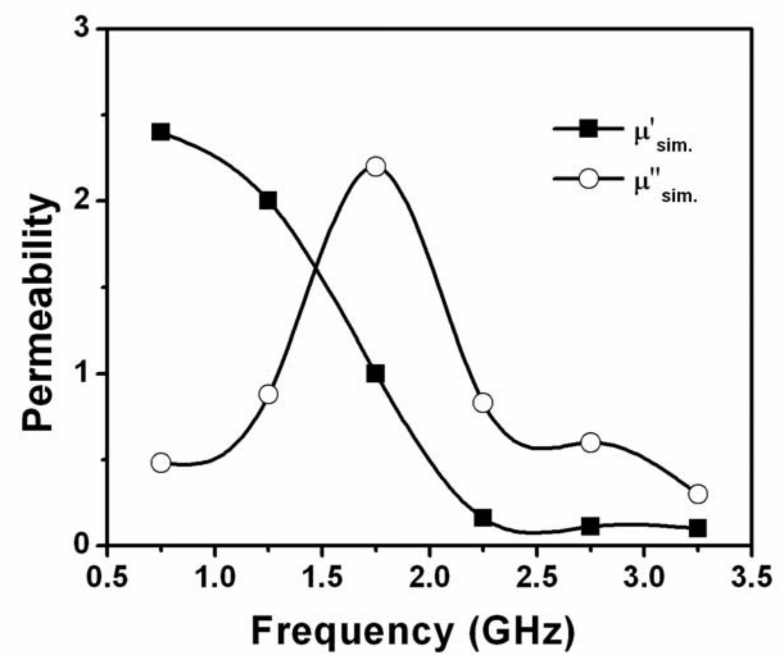

Figure 4.13 Simulation results of permeability for FeTaN lamination stack

The magnitude of calculated S_{11} (using μ_{eff} from Eqs. 4.44) and measured S_{11} results are compared in Fig. 4.11. The difference between calculated and measured magnitude values of S_{11} is smaller than 0.15. One possible reason for the difference is that the quasi-TEM mode approximation is not precise due to the neglect of higher propagation mode in the calculation process. Therefore, the effective permeability values need optimization by the parameter scanning function in HFSS software. The S_{11} variations with the permeability at 1.25 GHz are shown in Fig. 4.12. The difference between calculated and measured result is smaller than 0.13 when real permeability changes. And the phase of S_{11} is mainly affected by real permeability value at this frequency. When the real permeability is equal to 2, and the imaginary permeability changes from 0.6 to 0.88, $\left|S_{11}^{cal} - S_{11}^{mea}\right| < 0.1\,\mathrm{dB}$. Meanwhile, the phase of S_{11} keeps almost the same. As for other frequencies, the simulated effective permeability value can be seen in Fig. 4.13.

4.2.2.2 Transmission line method

i. Microstrip transmission line

In this section, we introduce a microstrip transmission line fixture to measure the permittivity and permeability of material at one time. We apply the measured scattering parameters (S_{11}, S_{21}) to calculate the complex permittivity (ε) and permeability (μ) of material. The result is also examined by the full wave electromagnetic analysis combined with an optimization procedure using commercial HFSS software.

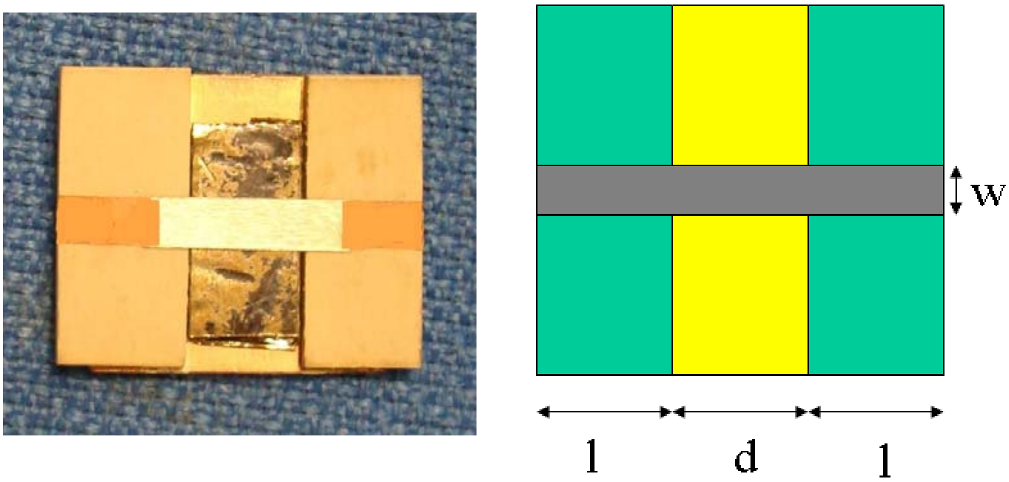

Figure 4.14 Fixture of microstrip transmission line cell

The measurement fixture is shown in Fig. 4.14. The cell consists of three portions: two portions of the low permittivity (relative permittivity $\varepsilon_r=2.94-0.0012j$ at 10 GHz made by Rogers 6002 PCB board) portion and the empty portion for loading sample. The low permittivity portion has a characteristic impedance of 50Ω determined by HFSS software. The cell dimensions are marked in Fig. 4.14, w=3.9 mm, d=9 mm, l=10 mm, and the height of the cell is 1.524mm. The *S*-parameter measurement was performed with a HP8722D network analyzer from 1.5 to 3.5 GHz. The Thru, Reflect, Line calibration was realized with the standard calibration kits to compensate the errors due to S-parameter test set and cables.

At low microwave frequencies, only quasi-transverse-electromagnetic (TEM) mode propagates along the transmission line. The characteristic parameters for deriving materials' properties mainly include characteristic impedance Z_C, propagation constant γ, effective permittivity ε_{eff}, and effective permeability μ_{eff}. These parameters are related by the following equations [12]

$$Zc = Z_0\sqrt{\frac{\mu_{eff}}{\varepsilon_{eff}}} \tag{4.45}$$

$$\gamma = \omega\sqrt{\varepsilon_0\mu_0\varepsilon_{eff}\mu_{eff}} \tag{4.46}$$

$$\tan\delta_{eff} = q_{\tan\delta d}\tan\delta d + q_{\tan\delta m}\tan\delta m \tag{4.47}$$

where

$$Z_0 = \frac{376.73}{2\pi}\ln\left[\frac{6+(2\pi-6)\exp[-(\frac{30.666}{u})^{0.7528}]}{u} + \sqrt{1+(\frac{2}{u})^2}\right] \tag{4.48}$$

$$\tan\delta d = \varepsilon''/\varepsilon' \tag{4.49}$$

$$\tan\delta m = \mu''/\mu' \tag{4.50}$$

$$q\tan\delta d = (1-(\varepsilon_{eff}^{'})^{-1})/(1-(\varepsilon')^{-1}) \tag{4.51}$$

$$q\tan\delta m = (1-\mu_{eff}^{'})/(1-\mu') \tag{4.52}$$

Where Z_0 is the characteristics impedance of microstrip in the medium ($\mu_r = \varepsilon_r = 1$). ($\varepsilon$', ε", μ', μ") are the relative permittivity and permeability of test sample.

According to Nicolson-Ross-Weir (NRW) method [13, 14], the relationship between propagation constant γ, characteristic impedance (Z_{cd}) of test sample and scattering parameter (S_{11}, S_{21}) (measured at coaxial-to-strip junction) is given by

$$\Gamma = \frac{Z_c - Z_{cd}}{Z_c + Z_{cd}} \tag{4.53}$$

$$z = \exp(-\gamma' l) \tag{4.54}$$

$$S_{11} = e^{-2\gamma d} \times \frac{(1-z^2)\Gamma}{1-\Gamma^2 z^2} \tag{4.55}$$

$$S_{21} = e^{-2\gamma d} \times \frac{(1-\Gamma^2)z}{1-\Gamma^2 z^2} \tag{4.56}$$

Where γ and γ' are the propagation constant of the low permittivity portion and sample portion, and Γ are the reflection coefficient at interface between the low permittivity portion and sample portion. And γ can be obtained by shorting the strip at the interface between the low permittivity portion and sample portion.

$$S_{11}^{air} = -\exp(-2\gamma d) \tag{4.57}$$

The analytic equation for magnetic case, the effective equation and the dispersion function can be defined as [15, 16]

$$\varepsilon_{eff}^{'} = \frac{1+\varepsilon'}{2}\left(\frac{A}{A-B}\right)^2 \tag{4.58}$$

$$\mu_{eff}^{'} = \frac{2\mu'}{1+\mu'}\left(\frac{A-B'}{A}\right)^2 \tag{4.59}$$

Where

$$A = \ln\frac{8h}{w} + \frac{1}{32}\left(\frac{w}{h}\right)^2 \tag{4.60}$$

$$B = \ln(\frac{\varepsilon'-1}{\varepsilon'+1})[\ln(\frac{\pi}{2}) + \frac{1}{\varepsilon'}\ln(\frac{4}{\pi})] \quad (4.61)$$

$$B' = \ln(\frac{\mu'-1}{\mu'+1})[\ln(\frac{\pi}{2}) + \mu\ln(\frac{4}{\pi})] \quad (4.62)$$

Therefore, (ε', ε", μ', μ") of test sample can be determined from S_{21} and S_{11} using above equations. However, the propagation mode in the microstrip line cell is not a strict TEM mode. Furthermore, the imperfection of test fixture will increase the errors of S_{21} and S_{11}, which will influence the uncertainty of (ε', ε", μ', μ") calculation result [17, 18]. Thus, a full wave electromagnetic analysis is needed to determine the accurate value of μ_{eff}. HFSS software was employed to electromagnetic analysis and optimization procedure. Above calculated (ε', ε", μ', μ") value were used in the simulation as the initial value. The optimized effective permeability value is valid only when simulated and measured magnitude and phase values of the S_{11}, S_{21} are reasonably close,

$\left|S_{11}^{\exp} - S_{11}^{sim}\right| \le 0.2dB$ (for dielectric material), 2 dB(for magnetic material)

(4.63)

$$\left|S_{21}^{\exp} - S_{21}^{sim}\right| \le 0.1dB \quad (4.64)$$

Where S_{11}^{sim} and S_{21}^{sim} are obtained by HFSS simulation; $S_{11}^{\exp}$ and $S_{21}^{\exp}$ are the experiment result.

ii Experiment results

The microstrip transmission line measurement and waveguide measurement performed on dielectric powder ($\varepsilon_r = 2.5 - 0$ j) are represented in Fig. 4.15. The measured (ε", μ', μ") values for dielectric powder corresponded to those anticipated.

Compared to the manufacture value, these values show an error better than 6%. However, large difference (about 10%) is also shown for real permittivity (ε') of dielectric powder. Such difference in ε' might be ascribed to several possible reasons. First, the composition (the ratio of dielectric powder and air) of the powder stack for microstrip measurement and waveguide measurement is different. Second, the imperfection of test fixture (especially the inevitable deformation of upper strip) will affect the measured scattering parameters. Third, the difference between real test fixture and models in HFSS software also influences the accuracy.

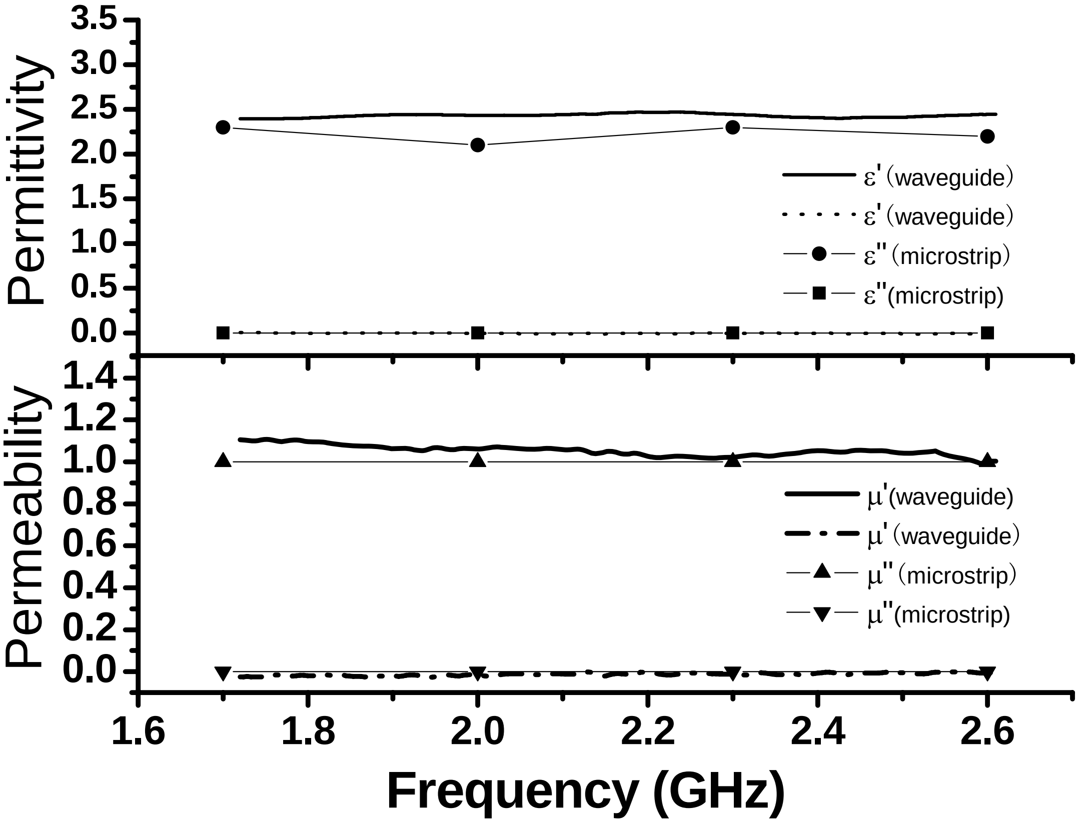

Figure 4.15 Measured complex permeability and permittivity value for dielectric powder ($\varepsilon_r = 2.5 - 0\,j$)

Measured and values for a FeTaN lamination stack are shown in Fig. 4.16. As it can be seen, with the frequency increase, the real permittivity ε' of stack decrease from 5 to 4.5, the imaginary permittivity ε" increase from 0 to 0.5, which are large than those obtained with the APC 7mm coaxial method with complex permittivity equaling to $4.2 - 0.2j$. The real permeability μ' decrease from 1.5 to 0.1, the imaginary permeability μ" shows a maximum value between 2.5 to 3 GHz. In principle, the large difference between S_{11}^{sim} and $S_{11}^{\exp}$ will increase the uncertainty of permeability and permittivity value, as shown in ref [19]. The dielectric loss, magnetic loss and whole microstrip cell losses affected measured (S_{11}, S_{21}) value and this will inverse increase the error of (ε', ε", μ', μ"). The inevitable strip deformation also influences the accuracy of result.

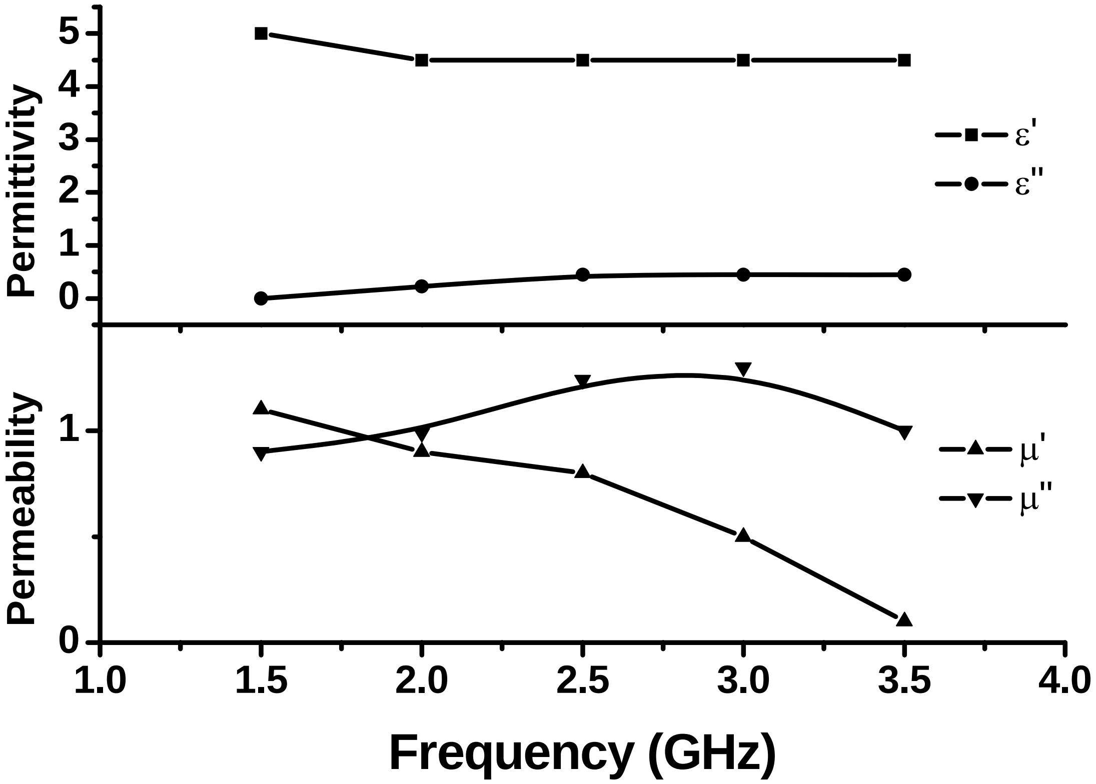

Figure 4.16 Measured complex permeability and permittivity value for FeTaN lamination stack

4.3 Waveguide transmission line measurement method

The diagram of waveguide and measurement fixture is shown in Fig. 4.17.

Waveguide measurement is widely used in application. Compared with microstrip measurement methods, it needs larger size sample due to its larger cross-section size.

4.3.1 Theory of waveguide transmission line [4]

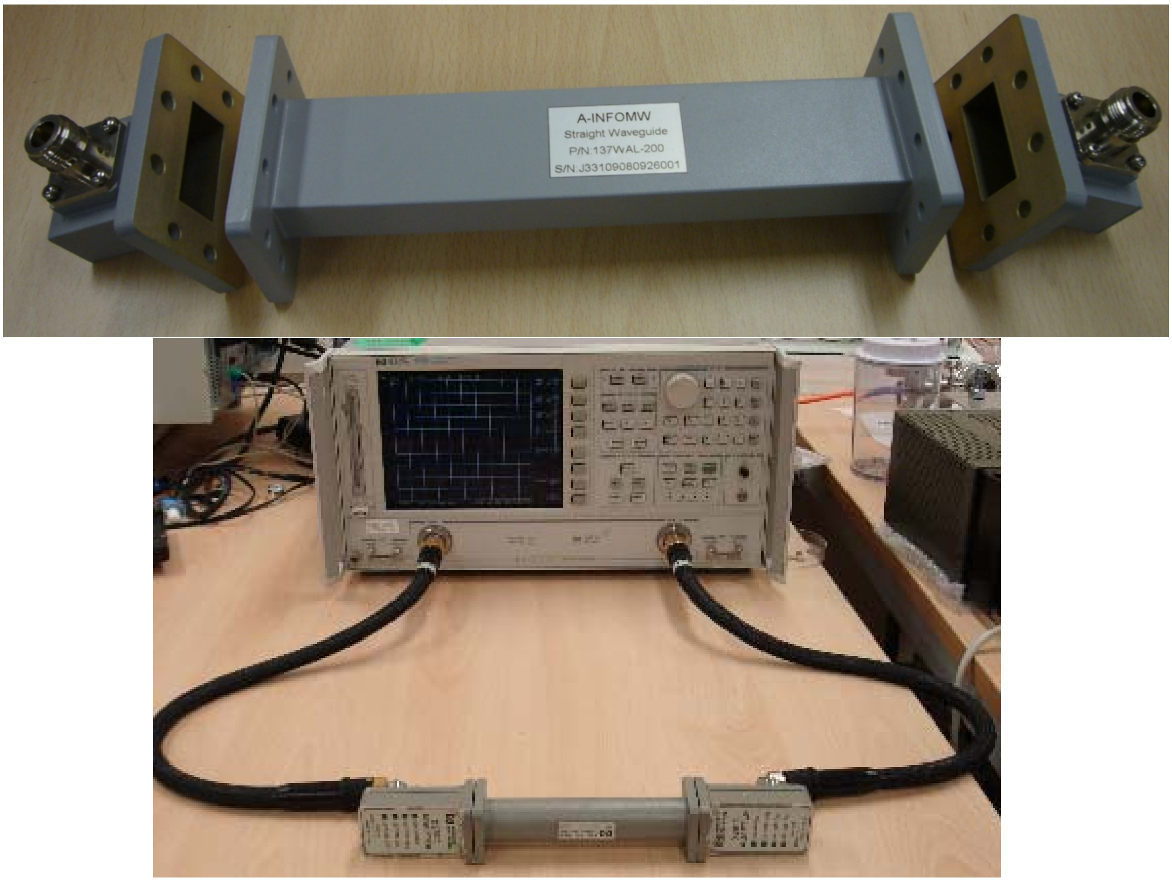

Figure 4.17 waveguide (C-Band) and measurement fixture for X-Band

For a time-harmonic field with an $e^{j\omega t}$ dependence wave propagation along the +z direction, the electric and magnetic fields can be written as:

$$\overline{E}(x,y,z) = [\overline{e}(x,y) + \hat{z}e_z(x,y)]e^{-j\beta z} \qquad (4.65)$$

$$\overline{H}(x,y,z) = [\overline{h}(x,y) + \hat{z}h_z(x,y)]e^{-j\beta z} \qquad (4.66)$$

Where $\overline{e}(x,y)$ and $\overline{h}(x,y)$ represent the transverse (x, y direction) electric and magnetic field components, while e_z and h_z are the longitudinal electric and magnetic field components. β is propagation constant for losses medium in the waveguide. If conductor or dielectric loss is present, the propagation constant will become $\gamma = \alpha + j\beta$, where α is damping factor.

If the transmission line or waveguide region is source free, Maxwell's equations can be written as

$$\nabla \times \overline{E} = -j\omega\mu\overline{H} \tag{4.67}$$

$$\nabla \times \overline{H} = j\omega\varepsilon\overline{E} \tag{4.68}$$

With an $e^{-j\beta z}$ z dependence, the three components of each of the above equations can be reduced to the following:

$$\frac{\partial E_z}{\partial y} + j\beta E_y = -j\omega\mu H_x \tag{4.69}$$

$$-j\beta E_x - \frac{\partial E_z}{\partial x} = -j\omega\mu H_y \tag{4.70}$$

$$\frac{\partial E_y}{\partial x} - \frac{\partial E_x}{\partial y} = -j\omega\mu H_z \tag{4.71}$$

$$\frac{\partial H_z}{\partial y} + j\beta H_y = j\omega\varepsilon E_x \tag{4.72}$$

$$-j\beta H_x - \frac{\partial H_z}{\partial x} = j\omega\mu E_y \tag{4.73}$$

$$\frac{\partial H_y}{\partial x} - \frac{\partial H_x}{\partial y} = j\omega\varepsilon E_z \tag{4.74}$$

The above six equations can be solved for the four transverse field components in terms of E_z and H_z as follows:

$$H_x = \frac{j}{k_c^2}(\omega\varepsilon \frac{\partial E_z}{\partial y} - \beta \frac{\partial H_z}{\partial x}) \tag{4.75}$$

$$H_y = \frac{-j}{k_c^2}(\omega\varepsilon \frac{\partial E_z}{\partial x} + \beta \frac{\partial H_z}{\partial y}) \tag{4.76}$$

$$E_x = \frac{-j}{k_c^2}(\beta \frac{\partial E_z}{\partial x} + \omega\varepsilon \frac{\partial H_z}{\partial y}) \tag{4.77}$$

$$H_x = \frac{j}{k_c^2}(-\beta \frac{\partial E_z}{\partial y} + \omega\mu \frac{\partial H_z}{\partial x}) \tag{4.78}$$

Where $k_c^2 = k^2 - \beta^2$.

Transverse electric (TE) wave, are characterized by $E_Z=0$ and $H_Z \neq 0$. Equations then reduced to

$$H_x = \frac{-j\beta}{k_c^2}\frac{\partial H_z}{\partial x} \tag{4.79}$$

$$H_y = \frac{-j\beta}{k_c^2}\frac{\partial H_z}{\partial y} \tag{4.80}$$

$$E_x = \frac{-j\omega\mu}{k_c^2}\frac{\partial H_z}{\partial y} \tag{4.81}$$

$$E_y = \frac{j\omega\mu}{k_c^2}\frac{\partial H_z}{\partial x} \tag{4.82}$$

In this case, $k_c \neq 0$, and the propagation constant is generally a function of frequency and the geometry of the line or guide.

The transverse field components of the TE_{mn} mode can be found as follows:

$$E_x = \frac{j\omega\mu n\pi}{k_c^2 b} A_{mn} \cos\frac{m\pi x}{a} \sin\frac{n\pi y}{b} e^{-j\beta z} \tag{4.83}$$

$$E_y = \frac{-j\omega\mu m\pi}{k_c^2 a} A_{mn} \sin\frac{m\pi x}{a} \cos\frac{n\pi y}{b} e^{-j\beta z} \tag{4.84}$$

$$H_x = \frac{j\beta m\pi}{k_c^2 a} A_{mn} \sin\frac{m\pi x}{a} \cos\frac{n\pi y}{b} e^{-j\beta z} \tag{4.85}$$

$$H_y = \frac{j\beta n\pi}{k_c^2 b} A_{mn} \cos\frac{m\pi x}{a} \sin\frac{n\pi y}{b} e^{-j\beta z} \qquad (4.86)$$

$$H_z(x,y) = A_{mn} \cos\frac{m\pi x}{a} \cos\frac{n\pi y}{b} e^{-j\beta z} \qquad (4.87)$$

Where a, b are the waveguide cross-section demission. Amn is arbitrary amplitude constant composed of the remaining constants A and C.

The propagation constant is

$$\beta = \sqrt{k^2 - k_c^2} = \sqrt{k^2 - (\frac{m\pi}{a})^2 - (\frac{n\pi}{b})^2} \qquad (4.88)$$

Only real β can propagation along the waveguide, which needs

$$k \ge k_c = \sqrt{(\frac{m\pi}{a})^2 + (\frac{n\pi}{b})^2} \qquad (4.89)$$

Each mode has the cutoff frequency f_{cmn} given by

$$f_{cmn} = \frac{\sqrt{(\frac{m\pi}{a})^2 + (\frac{n\pi}{b})^2}}{2\pi\sqrt{\mu\varepsilon}} \qquad (4.90)$$

Thus the TE_{10} mode is the dominant TE mode, and we will see, the overall dominant mode of rectangular waveguide. As a given operating frequency f, only modes having $f_{cmn}<f$ will propagate; Propagate with $f_{cmn}>f$ will lead to an imaginary, meaning that all field components will decay exponential away from the source of excitation.

In the vast majority of applications the operating frequency and guide dimensions are chosen so that only the dominant TE_{10} mode will propagate. Because of the practical importance of TE_{10} mode, we will list the field components and derive the attenuation due to conductor loss for this case.

Specializing to m=1, n=0 cases give the following results for the TE_{10} mode fields:

$$E_x = E_z = H_y = 0 \qquad (4.91)$$

$$H_z = A_{10} \cos\frac{\pi x}{a} e^{-j\beta z} \qquad (4.92)$$

$$E_y = \frac{-j\omega\mu a}{\pi} A_{10} \sin\frac{\pi x}{a} e^{-j\beta z} \qquad (4.93)$$

$$H_x = \frac{j\beta a}{\pi} A_{10} \sin\frac{\pi x}{a} e^{-j\beta z} \qquad (4.94)$$

The lowest f_c occurs for TE_{10} (m=1, n=0) mode for a>b:

$$f_{c10} = \frac{1}{2a\sqrt{\mu\varepsilon}} \qquad (4.95)$$

$$k_c = \frac{\pi}{a} \qquad (4.96)$$

The guide wavelength λ_g is defined as the distance between two equal phase plane along the waveguide, and is equal to

$$\lambda_g = \frac{2\pi}{\beta} \qquad (4.97)$$

$$\beta = \sqrt{k^2 - (\frac{\pi}{a})^2} \qquad (4.98)$$

The characteristic impedance of an air-filled section of rectangular waveguide is

$$Z_{air} = \sqrt{\frac{\mu_0}{\varepsilon_0}} \frac{\lambda_g}{\lambda_0} \qquad (4.99)$$

$$\lambda_g = \frac{\lambda_0}{\sqrt{1 - (\frac{\lambda_0}{\lambda_c})^2}} \qquad (4.100)$$

Where λ_c is the low-frequency cutoff wavelength of the TE_{10} mode, λ_0 is free space wavelength.

While the sample was loaded in the waveguide, the propagation constant β needs to be replaced by $\gamma_{guide} = \alpha + j\beta$. The characteristic impedance of the sample-filled section is given.

$$Z_{sample} = j\frac{2\pi f\mu_r\mu_0}{\gamma_{guide}} \qquad (4.101)$$

Where $\gamma_{guide}^2 = (\frac{2\pi}{\lambda_c})^2 - (\frac{2\pi\sqrt{\mu\varepsilon}}{\lambda_0})^2$ (4.102)

And $\mathrm{Im}\,a(2\pi/\gamma_{guide}) = \lambda_g$ (4.103)

4.3.2 Measurement Procedures

According to Nicolson-Ross-Weir method, the relationship between propagation constant γ, normalized characteristic impedance Z, the reflection coefficient Γ of test sample and scattering parameter (S_{11}, S_{21}) is shown in Fig 4.18.

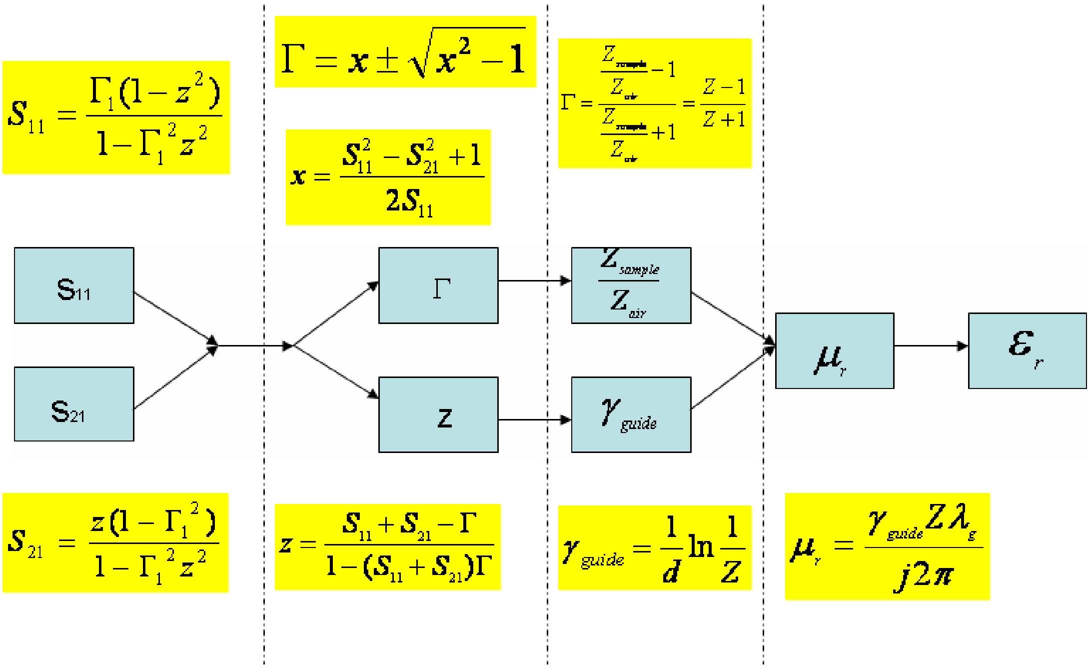

Figure 4.18 Calculation procedures for permeability and permittivity

From the measured S_{21} and S_{11}, the normalized characteristic impedance Z and γ_{guide}

are calculated. For the portion filled by sample,

$$Z = \frac{Z_{sample}}{Z_{air}} = j\frac{2\pi f\mu_r\mu_0}{\gamma_{guide}} \times \frac{\lambda_0}{\lambda_g}\sqrt{\frac{\varepsilon_0}{\mu_0}} \qquad (4.104)$$

Therefore, the permeability of sample, $\mu_r = \frac{\gamma_{guide} Z \frac{\lambda_g}{\lambda_0}}{j\frac{2\pi}{\lambda_0}}$.

The material refractive index N_m is

$$Nm = \frac{1}{j\frac{2\pi}{\lambda_0}}\sqrt{\gamma_{guide}^2 - (\frac{2\pi}{\lambda_c})^2} = \sqrt{\mu_r\varepsilon_r} \qquad (4.105)$$

Then, the permeability of sample, $\varepsilon_r = \frac{N_m^2}{\mu_r}$.

The permeability and permittivity of commercial absorber (ECCOSORB-SS6M) in X-band is shown in Fig. 4.19. The result is food agreement with HFSS simulation for EM absorber in X-band.

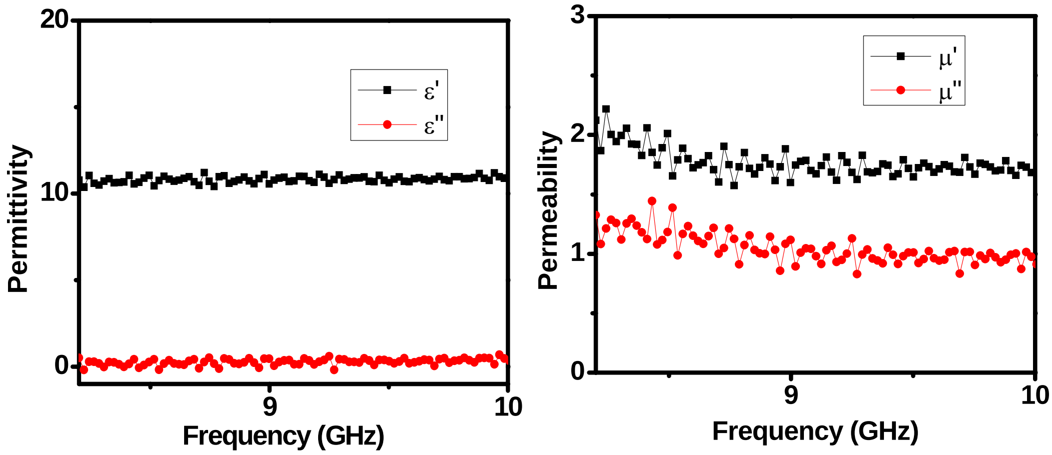

Figure 4.19 Permeability and permittivity of commercial absorber (ECCOSORB)

Reference

[1] A. L. Adenot, O. Acher, T. Taffary, P. Quéffélec, and G. Tanné, J. Appl. Phys. **87**, 6914 (2000).

[2] Y. G. Ma and C. K. Ong, J. Phys. D **40**, 3286 (2007).

[3] Stephen C. Harsany, Principles of Microwave Technology (Prentice-Hall, Inc, 1997).

[4] D. M. Pozar, Microwave Engineering (Wiley, New York, 2005).

[5] J. Hinojosa, IEEE Microw. Wirel. Compon. Lett. **11**, 305 (2001).

[6] Y. Liu, L. F. Chen, C. Y. Tan, H. J. Liu, and C. K. Ong, Rev. Sci. Instrum. **76**, 063911 (2005).

[7] L. M. Brekhovskih, Waves in Layered Media (Academic, New York, 1960).

[8] P. Quéffélec, M. Le Floćh, and P. Gelin, IEEE Trans. Instrum. Meas. **47**, 956 (1998).

[9] P. Quéffélec, P. Gelin, J. Gieraltowski, and J. Loaec, IEEE Trans. Magn. **30**, 224 (1994).

[10] P. Quéffélec, IEEE Trans. Microwave Theory Tech. **50**, 2128 (2002)

[11] S. Dubourg, S. Queste, and O. Acher, J. Appl. Phys. **97**, 10F903 (2005).

[12] R. A. Pucel and D. J. Masse, IEEE Trans. Microwave Theory Tech. **MTT-20**, 304 (1972).

[13] W.B.Weir, Proc. IEEE **62**, 33 (1974).

[14] A. M. Nicolson and G. Ross, IEEE Trans. Instrum. Meas. **IM-19**, 377 (1970).

[15] E. Hammerstad and O. Jensen, IEEE MTT-S Int. Microwave Symp. Digest, 407

(1980).

[16] M. Kirschning and R. H. Jansen, Electron. Lett. **18**, 272 (1982).

[17] E. J. Denlinger, IEEE Trans Microwave Theory Tech. **MTT-28**, 513 (1980).

[18] L. Lewin, Proc. Inst. Elect. Eng. **125**, 633 (1978).

[19] A. Boughriet, C. Legrand, and A. Chapoton, IEEE Trans. Microwave Theory Tech. **45**, 52 (1997).

CHAPTER 5

CONCLUSION

In this thesis, the patterning method was utilized to improve the resonance frequency of nanocrystalline FeTaN thin film, which had large permeability (10^3) up to ~1 GHz. The magnetic properties and microwave response of the patterned strip arrays were investigated at different strip widths and patterning directions.

We also deposit FeTaN thin films on flexible insulator polymer substrates and glue them together to form a composite material consisting of ferromagnetic films laminated with insulating polymer sheets. The fabrication of this kind of soft magnetic lamination stacks makes them a good candidate for high-frequency microwave device applications.

In this thesis, we develop shorted microstrip transmission line method, and apply these methods to measure the scattering parameters of the FeTaN lamination stack. Permeability spectra of the FeTaN lamination stack are obtained by the shorted load transmission line model. In data processing procedure, the effective permeability of the FeTaN lamination stack at different frequencies describing the transmission line is determined from the reflection measurements at different measurement frequencies. The result is examined by the full wave electromagnetic analysis combined with an optimization procedure using commercial HFSS software.

We develop microstrip transmission line method to obtain the complex permeability and permittivity spectra of the FeTaN lamination stack. In data processing procedure, the effective permeability of the FeTaN lamination stack at different frequencies describing the transmission line is determined from the (S_{21}, S_{11}) at different measurement frequencies. The result is examined by the full wave electromagnetic analysis combined with an optimization procedure using commercial HFSS software. And the result error is larger than shorted microstrip transmission line.

We also employed micrtostrip perturbation method to measure single layer FeTaN films. Waveguide method also was employed to measure other bulk materials.

Appendix A

MICROSTRIP CALIBRATION SEQUENCE INPUT IN VNA

A.1 Input new Sequence for microstrip transmission line calibration

1. Press Seq.
2. Select:
    a. NEW SEQ
    b. SEQUENCE 6 (for new sequence)
3. Press Cal
4. Select:
    a. CAL KIT
    b. SELECT CAL KIT
    c. USER KIT
    d. RETURN
5. Press MODIFY
6. Press DEFINE STANDARD
7. Select:
    a. Press 1×1 (the calibration standard number), the softkey THRU is underlined. Press THRU.
    b. MODIFY STANDARD DEFINETION.
    c. SPECIFY OFFSET.

  d. OFFSET DELAY, and enter the new offset delay (0 ps).

  e. OFFSET LOSS, and enter the new offset loss (0 GΩ/s).

  f. OFFSET Z_0, and enter the new Z_0 (50 Ω).

  g. MINIMUM FREQUENCY, and enter the new cutoff frequency (0GHz).

  h. MAXiMUM FREQUENCY, and enter the new maximum frequency (999GHz).

  i. COAX

  j. Standard DONE

8. Press DEFINE STANDARD

9. Select:

   a. Press 2×1 (the calibration standard number), the softkey SHORT is underlined. Press SHORT.

   b. MODIFY STANDARD DEFINETION.

   c. SPECIFY OFFSET.

   d. OFFSET DELAY, and enter the new offset delay (-22.5 ps).

   e. OFFSET LOSS, and enter the new offset loss (0 GΩ/s).

   f. OFFSET Z_0, and enter the new Z_0 (50Ω).

   g. MINIMUM FREQUENCY, and enter the new cutoff frequency (0GHz).

   h. MAXiMUM FREQUENCY, and enter the new maximum frequency (999GHz).

   i. COAX

   j. Standard DONE

10. Press DEFINE STANDARD.

11. Select:

a. Press 3×1 (the calibration standard number), the softkey DELAY/THRU is underlined. Press DELAY.

b. MODIFY STANDARD DEFINETION.(1.99 GHz-18.1 GHz ICM LINE2 for example)

c. SPECIFY OFFSET.

d. OFFSET DELAY, and enter the new offset delay (22.5 ps).

e. OFFSET LOSS, and enter the new offset loss (0 GΩ/s).

f. OFFSET Z_0, and enter the new Z_0 (50 Ω).

g. MINIMUM FREQUENCY, and enter the new cutoff frequency (1.99 GHz).

h. MAXiMUM FREQUENCY, and enter the new maximum frequency (18.1 GHz).

i. COAX

j. Standard DONE

12. Press SPECIFY CLASS

13. Select:

a. S11A, press 1×1, 2×1, 3×1.

b. S11B, press 1×1, 2×1, 3×1.

c. S11C, press 1×1, 2×1, 3×1.

d. S22A, press 1×1, 2×1, 3×1.

e. S22B, press 1×1, 2×1, 3×1.

f. S22C, press 1×1, 2×1, 3×1.

14. press MORE.

15. Select:

    a. FWD TRANS, press 1×1, 3×1.

    b. REV TRANS, press 1×1, 3×1.

    c. FWD MATCH, press 1×1, 3×1.

    d. REV MATCH, press 1×1, 3×1.

    e. RESPONSE, press 1×1, 3×1.

    f. RESPONSE&ISOL’N, press 1×1, 3×1.

16. press MORE

    a. TRL THRU, press 1×1.

    b. TRL REFLECT, press 2×1.

    c. TRL LINE OR MATCH, press 3×1.

17. Press SPECIFIC CLASSIC DONE.

18. Press KIT DONE.

19. Press SAVE USER KIT.

20. Press Seq

21. Press DONE SEQUENCE MODIFY.

A.2 Performing a Calibration for microstrip trasnsmission line

1. Press Seq.

2. Select

    a. DO SEQUENCE.

b. SEQUENCE 6.

4. Set START and STORP frequency.

5. Press Cal.

6. Press CAL MENU.

7. Press TRL.

8. Follow the prompts on the display.

PAPER PUBLISHED

1. **Chen X**; Ma YG; Xu F; Wang P; Ong CK, ‘A broadband permeability measurement of FeTaN lamination stack by the shorted microstrip line method’(J. Appl. Phys. , 105 (2009) 013904)
2. Zhao L.**, Chen X,** C. K. Ong**,** ‘Visual observation and quantitative measurement of the microwave absorbing effect at X band’ (Review of Scientific Instruments 79 (2008) 124701)
3. Xu F; **Chen X**; Ma YG; Phuoc NN; Zhang XY; Ong CK, ‘Influence of Si concentration on the magnetization dynamics in as-sputtered FeCoSiN thin films at high frequencies’ (J. Appl. Phy*s.* 104 (2008) 083915)
4. **Chen X**; Ma YG; Ong CK, ‘Magnetic anisotropy and resonance frequency of patterned soft magnetic strips’ (J. Appl. Phys. 104 (2008) 013921)
5. Tan, CY; **Chen, X**; Ma, YG; Liu, Y; Liu, ZW; Ong, CK, ‘Ferromagnetic resonance frequency tuning of FeTaN thin films by strips patterning with angular displacements’ (J. Phys. D: Appl. Phys. 40 (2007) 6888)